Applied Thermal Engineering 181 (2020) 115966

Contents lists available at ScienceDirect

Applied Thermal Engineering

journal homepage: www.elsevier.com/locate/apthermeng

Effect of inlet subcooling on flow boiling in microchannels

Vivian Y.S. Lee, Tassos G. Karayiannis*

Department of Mechanical and Aerospace Engineering, Brunel University London, Uxbridge UB8 3PH, UK

HIGHLIGHTS

- Increasing subcooling reduced the range for active nucleation sites in flow boiling.
- Microchannel flow patterns and two-phase instability affected by subcooling.
- Heat transfer rates affected by inlet degree of subcooling.
- Two-phase pressure drop decreases with increasing subcooling at a given heat flux.
- Influence of subcooling may explain discrepancies in microchannel flow boiling data.

ARTICLE INFO

Keywords:
Flow boiling
Microchannels
Inlet subcooling

ABSTRACT

The paper describes experimental work to assess the effect of inlet subcooling on the flow boiling characteristics of HFE-7200 in a multi-microchannel heat sink. The experiments were performed at a mass flux of 200 kg/m^2 s and system pressure of 1 bar for inlet subcooling conditions of 5 K, 10 K and 20 K and wall heat flux between 25.9 and 180.7 kW/m^2. The equivalent base heat flux was between 99.1 and 605.3 kW/m^2. The microchannel evaporator had 44 channels which were 0.36 mm in width and 0.7 mm in depth. The thickness of the fin between the channels was 0.1 mm and the base area of the microchannels was 20 mm × 20 mm. Increasing inlet subcooling generally decreased two-phase pressure drop in the channels and delayed flow regime transitions in the heat sink. Flow instability was also found to be dependent on the degree of inlet subcooling. The extended subcooled region of the channels at higher degrees of subcooling resulted in lower average heat transfer coefficients in the heat sink, especially at low heat fluxes. The effect of inlet subcooling on local heat transfer coefficients was less pronounced in the saturated boiling region. The study verified the importance of the degree of subcooling when comparing heat transfer and pressure drop characteristics in microchannel heat sinks and when optimising the design of integrated thermal management systems for high heat flux electronic devices.

1. Introduction

High heat fluxes in modern electronics pose a significant thermal management challenge, not merely in terms of chip-level power dissipation, but also at system-level heat rejection from electronics packages to the ambient. Chip-level power densities are projected to be as high as 4.5 MW/m^2 in computing platforms by 2026 [1] and have been reported to exceed 10 MW/m^2 in power modules for defence applications [2]. For instance, microwave power modules used in critical applications such as radar systems and satellites operate at high frequencies to improve dynamic response and reduce component size, albeit at the cost of device efficiency. For a typical efficiency of 20% and input power of 850 W, almost 700 W of waste heat must be rejected from the system into the immediate environment, proving to be very challenging. Although air cooling is a popular thermal management technique in many of the aforementioned industries due to ease of application, air cooling assemblies have generally been reported to be inadequate for heat fluxes above 1–1.5 MW/m^2 as they begin to approach their volumetric footprint and acoustic limits as well as being difficult to integrate on multi-core boards [3–5]. On the other hand, flow boiling in microchannels is regarded as a promising cooling solution [1]. for microelectronic systems where junction temperatures are limited to between 85 °C and 125 °C.

Microchannel liquid cooling was first introduced by Tuckerman and Pease [6] in the early 1980 s and has since been extensively studied for the cooling of miniaturised technologies [7–9]. The water-cooled silicon microchannel heat sink (base area of 1 × 1 cm^2) studied in [6] achieved a maximum heat flux of 7.9 MW/m^2, albeit at a relatively

* Corresponding author.
E-mail address: tassos.karayiannis@brunel.ac.uk (T.G. Karayiannis).

https://doi.org/10.1016/j.applthermaleng.2020.115966
Received 8 May 2020; Received in revised form 24 July 2020; Accepted 24 August 2020
Available online 30 August 2020

Nomenclature

B	constant in Eq. (23), given in Eq. (24)
C^+	dimensionless constant in Eq. (16), [–]
c_p	specific heat capacity, [J/kg K]
D_h	hydraulic diameter, [m]
f	friction factor, [–]
$(fRe)_{fd}$	fully-developed Poiseuille number in Eq. (16), [–]
G, G_{ch}	mass flux in the channels, [kg/m^2 s], $G_{ch} = \dot{m} / (N W_{ch} H_{ch})$
H	height, [m]
h, HTC	heat transfer coefficient, [W/m^2 K]
$\bar{h}$	average heat transfer coefficient, [W/m^2 K]
i	specific enthalpy, [J/kg]
i_{fg}	latent heat of vapourisation, [J/kg]
j	experimental parameter
k	thermal conductivity, [W/m K]
K(∞)	dimensionless constant in Eq. (16), [–]
L	length, [m]
L^+	dimensionless length in Eq. (16), [–]
MAE	mean average deviation, Eq. (33) [%]
m	fin parameter, [–]
$\dot{m}$	mass flow rate, [kg/s]
n	number of data collected, [–]
N	number of channels, [–]
Nu	Nusselt number, [–]
$\bar{Nu}$	average Nusselt number, [–]
P	pressure, [bar]
ΔP	pressure drop, [Pa]
q''	heat flux, [W/m^2]
R_a	average surface roughness, [μm]
r_c	cavity radius in Hsu's model given in Eq. (34), [m]
Re	Reynolds number in the channels, [–],Re = $(G_{ch} D_h) / \hat{I}¼_f$
T	temperature, [K]
ΔT_{sub}	temperature difference, [K],$\Delta T_{sub} = T_{sat,p_i} - T_i$
ΔT_{sup}	degree of wall superheat, [K], $\Delta T_{sup} = T_w - T_{sat}$
V	velocity, [m/s]
W	width, [m]
x	vapour quality, [–]
Y	vertical distance between thermocouples, [m]
z	axial location along channel, [m]
z/L	dimensionless axial location, [–]
σ(Δj)	standard deviation of experimental parameter

Greek symbols

σ	surface tension, [N/m]
α_p	plenum area ratio defined in Eq. (3) and (4), [–]
α_v	void fraction estimated by Eq. (27), [–]
β	area ratio defined in Eq. (5) and (6), [–]
δ_t	thermal boundary layer thickness, [m]
η	fin efficiency, [–]
ν	kinematic viscosity, [m$^{2/S}$]
ρ	density, [kg/m^3]

Subscripts

app	apparent
b	base
bd	bend
ch	channel
cu	copper
e	exit
f	liquid-phase
fin	fin between channels
fl	fluid line
g	gas-phase
i	inlet
ip	inlet plenum
op	outlet plenum
sat	saturated
sc	sudden contraction
se	sudden expansion
sp	single-phase
sub	subcooled
sup	superheat
tc	thermocouple
tp	two-phase
w	wall
z	axial location

large pressure drop of 204 kPa as well as a notable temperature rise across the substrate. The temperature rise of the substrate was 71 K with a water inlet temperature of 23 °C, resulting in chip temperatures of around 94 °C. By exploiting the latent heat of vapourisation of a fluid, heat transfer coefficients up to two orders of magnitude higher than forced liquid convection may be attained, achieving significantly higher heat dissipation capability at a given coolant flow rate [2,10]. A maximum heat flux of 7 MW/m^2 was attained using microchannel heat sinks of base area 5 mm × 10 mm in Lee and Mudawar [11] whilst Drummond et al. [12] managed heat fluxes up to 9.1 MW/m^2 by employing a hierarchical manifold design with dedicated fluid delivery to each microchannel heat sink in a novel 3 × 3 square array. It is important to note that flow boiling in microchannel heat sinks can potentially moderate temperature non-uniformities associated with sensible heat rise in single-phase microchannels as the vapourisation process occurs isothermally. Additionally, two-phase microchannel cooling could be more efficient in alleviating hotspots due to an increase in the heat transfer coefficient in response to heat flux, especially in the nucleate boiling regime [1]. Furthermore, the simple and compact system architecture of a two-phase microchannel heat sinks makes it comparable for embedded chip cooling applications to jet impingement and spray cooling nozzle modules, which have also been studied in boiling mode for high heat flux thermal management [13–15].

Despite many potential merits and proven high heat dissipation capability, flow boiling based evaporative cooling systems with microscale heat sinks have limited commercial availability. Industry trends remain slow in adopting two-phase microchannel cooling compared to its single-phase counterpart. One of the main challenges in flow boiling is the large scatter in flow boiling results, which hinders the establishment of generally accepted prediction methods in two-phase flow patterns, heat transfer, pressure drop and critical heat flux, as addressed in Karayiannis and Mahmoud [1], Kandlikar [16], Cheng and Xia [17] and most recently in Kutznetsov [18]. This is in part due to the unclear dependence of microchannel flow boiling behaviour on operational conditions, for instance, effect of heat flux, mass flux, system pressure and inlet subcooling and parameters such as surface finish, material, heated length and fluid properties [19,20]. Evidently, the effect of various operational parameters on the performance of the cooling system must be well understood to facilitate successful integration of the developed technology into real-life systems.

In spite of the fact that inlet conditions of the working fluid could significantly influence flow boiling in microchannels, there is a predominant lack of literature addressing its effect on the performance of microchannel heat sinks. The size range of effective cavities, based on the classical model by Hsu [21], is a function of subcooling degree. Similarly, Kandlikar [22] showed a high dependency of flow boiling

nucleation criteria, as well as flow boiling stability on bulk liquid subcooling. Accordingly, bubble growth and departure dynamics have been shown to vary with liquid subcooling, as discussed thoroughly in Euh et al. [23] and Goel et al. [24]. Even though these two studies were primarily concern with flow boiling at the macroscale level, the findings still indicate a potential influence of liquid subcooling on the nucleation characteristics in microscale flows. Bubble departure diameter and frequency were generally found to decrease with increase in subcooling degree (i.e. lower bulk fluid temperature). Lower bubble departure frequencies are caused by the longer waiting time between successive bubble ebullition cycles, as lower bulk liquid temperatures require a longer period in order to re-establish a certain degree of superheat at the wall for nucleation after bubble departure.

1.1. Effect of inlet subcooling on the onset of boiling

For microchannels, a delay in the onset of boiling from 1184 kW/m^2 to 1897 kW/m^2 was reported with increasing subcooling degree at a given flow rate in Lee and Mudawar [25] using HFE-7100 as the working fluid. Ong and Thome [26] investigated the influence of inlet subcooling, between 2 K and 9 K, on the flow boiling of refrigerant R134a, R245fa and R236fa in circular tubes covering the microscale range and reached the same conclusion, i.e. delayed onset of boiling with increasing subcooling. Additionally, Chen et al. [27] and Zhang et al. [28] both demonstrated a slightly higher boiling incipience wall superheat by around 2 K at higher inlet subcooling in a similar interconnected microchannel configuration using deionised water at subcooling conditions of 10, 40 and 70 K. Boiling incipience heat flux increased with subcooling in Deng et al. [29] in a re-entrant porous microchannel array, while Deng et al. [30] noted higher degrees of wall superheat, of around 4 K at boiling initiation at high subcooling conditions for the flow boiling of water and ethanol in an interconnected pin-fin heat sink. Zeng et al. [31] found that the wall superheat condition at the onset of nucleate boiling increased from 0.3 K to 4.9 K corresponding to an increase in inlet liquid subcooling from 10 K to 40 K for flow boiling of DI water in micro-grooved channels with secondary grooves as re-entrant cavities. From the above, it is clear that the degree of subcooling influences both the degree of superheat and the wall heat flux required for boiling incipience, although the work presented so far is not detailed or enough to quantify these changes.

1.2. Effect of inlet subcooling on flow instability

A number of researchers studied the effect of degree of subcooling on flow instabilities in microchannels. Prajapati and Bhandari [32] cited flow reversal and parallel channel interaction, for large inlet subcooling conditions, as major causes of flow instabilities in microchannels. However, past researchers gave contradictory statements on the dependence of flow instability on the degree of subcooling. Lee et al. [33] found with R134a that increasing inlet subcooling mitigated pressure drop oscillations in microchannels. The authors reasoned that low liquid inlet temperatures had a higher damping effect on vapour backflow into the inlet plenum. Pressure drop oscillations intensified intermittent dryout, which occurred predominantly in annular flow and degraded heat transfer coefficients appreciably in this region. Chen et al. [27] also reported lower two-phase oscillations including the inlet pressure and inlet temperature at higher inlet subcooling. This was attributed to the delayed transition to annular flow, a regime where flow reversal was typically observed in their heat sink.

On the contrary, high inlet liquid subcooling produced significant flow oscillations in [34–36]. Bogojevic et al. [34] studied the flow boiling of water in silicon microchannels at two inlet subcooling conditions (inlet temperatures 25 °C and 71 °C at an approximate inlet pressure of 1 bar) and found that the magnitude of temperature oscillations as well as temperature non-uniformity resulting from vapour backflow from the channel array to the inlet plenum were significantly amplified at higher liquid subcooling conditions. Similarly, more severe pressure and temperature fluctuations were recorded at lower water inlet temperatures in the study by Deng et al. [35] in both their plain microchannel and micro-pin fin structured microchannel heat sink . They compared results for inlet subcooling degrees of 10 K and 40 K using water and ethanol as the working fluid. Kingston et al. [36] studied the flow boiling of fluid HFE-7100 in a parallel microchannel heat sink and found high amplitude temperature oscillations at higher degrees of inlet subcooling. The instabilities were associated to rapid bubble growth in the channels.

The effect of inlet subcooling on flow instabilities is also dependent on fluid properties of the working fluid. Deng et al. [30] reported different subcooling effects using water and ethanol as working fluids in the same pin-fin re-entrant microchannel heat sink. Flow instabilities were aggravated using water with increase in inlet subcooling degree, whilst in ethanol higher inlet subcooling suppressed two-phase flow oscillations in the test section. The authors also noted that the amplitude of oscillations of ethanol were generally larger than that recorded using water. No justification was provided for the disparity between the two fluids. In summary, there are conflicting reports on the effect of the degree of inlet subcooling on flow instabilities in microchannels. Furthermore, the effect of fluid properties on the magnitude of the effect of the degree of subcooling is not clear.

1.3. Effect of inlet subcooling on heat transfer rates

Some past reports indicate an insignificant effect of subcooling on heat transfer coefficients, particularly in the saturated boiling region [26,37,38]. Agostini et al. [37] concluded that increasing inlet subcooling did not significantly affect heat transfer coefficients in the saturated region for subcooling conditions of 0.6 K to 18.3 K and from 0 K up to 19 K for refrigerant R245fa and R236fa respectively. The authors emphasised however, that in the subcooled region, increasing inlet subcooling resulted in a reduction in the heat transfer coefficients for both fluids. Similarly, a small effect of subcooling on local heat transfer coefficients at vapour qualities $x < 0.1$, influenced by the location of boiling incipience, as covered above, was also observed in Ong and Thome [26,38]. The same group, Huang and Thome [39], monitored the local heat transfer coefficient at a fixed location along their multi-microchannel heat sink and reported lower local heat transfer coefficients in the subcooled and saturated boiling region at higher inlet subcooling due to a corresponding extension of the subcooled region for refrigerants R245fa and R236fa.

Contrary to the above, research in enhanced or structured microchannel heat sinks typically concluded a positive effect of subcooling on heat transfer coefficients [27,29,35,40]. In an open microchannel configuration (i.e. cover plate does not completely seal on the top of the fins), Yin et al. [40] reported that increasing inlet subcooling delayed the occurrence of stratified flow, a flow regime prone to local wall dryout, and hence increased the local two-phase heat transfer coefficient assessed near the channel outlet. Chen et al. [27] sintered a porous copper layer on a microchannel heat sinks with square re-entrant cavities and found that increasing inlet subcooling delayed the development of annular flow, and thus liquid film dryout in the channels. When they presented the local two-phase heat transfer results at the most downstream location on the heat sink, an improvement in heat transfer with increase in inlet subcooling was demonstrated. Deng et al. [29] and Deng et al. [35] separately reported an increase in downstream (i.e. nearest to channel exit) heat transfer coefficients at higher subcooling.

Zeng et al. [31] recommended selecting an optimum liquid subcooling may also be used to control flow pattern development in the channels to benefit heat transfer performance. They studied a range of degree of subcooling at 10, 25 and 40 K for water. The highest two-phase heat transfer coefficient at the channel outlet was obtained at a medium inlet subcooling of 25 K, due to the persistence of stable

annular flow in their grooved microchannel array. The authors explained that at low inlet subcooling (at 10 K inlet subcooling), slug and annular flow developed early in the channels. A longer dryout period, which was assumed to be the cause of heat transfer deterioration, was observed downstream in the channels. Flow visualisation revealed that the dryout period persisted for 25 ms longer at 10 K compared to when subcooling was set to 25 K.

1.4. Effect of inlet subcooling on critical heat flux

Increasing inlet subcooling may also delay the occurrence of critical heat flux in microchannels, although this might only be relevant at very high degrees of subcooling. Lee and Mudawar [11] reported that for HFE-7100, the critical heat flux limit was extended to 4470 kW/m^2 at higher degree of subcooling (~90 K) from 3180 kW/m^2 (~60 K) for the subcooled flow boiling of HFE-7100 in a microchannel heat sink. Notice that the study by Lee and Mudawar [11] employed very high inlet subcooling degrees (60 K and 90 K). Deng et al. [29] studied the flow boiling of ethanol also at relatively large subcooling degrees of up to 40 K and also attained enhanced critical heat flux up to nearly 250 kW/m^2 at 40 K compared to 200 kW/m^2 at 10 K at set mass flux conditions. On the other hand, Revellin and Thome [41] in their theoretical model noted that the effect of subcooling is not significant at low values of inlet subcooling. Agostini et al. [42], for instance, found that the critical heat flux in their microchannel heat sink using R236fa was unaltered at subcooling degrees in the range of 0.4 K to 15.3 K. This agrees with the observation in Ong and Thome [38] for fluid R134a, R245fa and R236fa at subcooling degrees between 2 K and 9 K.

The above summary clearly indicates the existing disagreement among various research groups on the effect of inlet subcooling on heat transfer rates and critical heat flux. Firstly, past work is not conclusive on the effect of inlet subcooling on local and subsequently average heat transfer rates in microchannels and this calls for further work to be carried out. Secondly, past reports indicate that the critical heat flux can be affected by the degree of inlet subcooling if the differences in the actual degree of subcooling values are high. And again, further work is needed to actually quantify these changes.

1.5. Effect of inlet subcooling on two-phase pressure drop

Two-phase pressure drop generally decreased with increase in inlet subcooling [27,29]. Chen et al. [27], using water as the working fluid with an inlet pressure of approximately 1 bar, reported a reduction in flow boiling pressure drop from 5.5 kPa to 1.5 kPa when the inlet subcooling was increased from 10 K to 70 K. This was attributed to lower void fraction in the channels at higher subcooling. Deng et al. [29] reasoned that pressure drop in the two-phase region was lower due to the smaller two-phase region in the heat sink at higher subcooling conditions. Huang and Thome [43] investigated the effect of inlet subcooling of R245fa and R236fa at subcooling degrees of 5.5, 10 and 15 K, and demonstrated that there was a notable reduction of total pressure drop in the heat sink when the subcooling degree was increased from 5.5 K to 10 K, but did not vary with further increase in subcooling to 15 K. On the other hand, the pressure drop in the channel array, that is, the total pressure drop corrected for inlet and outlet restriction pressure losses, increased with increase in subcooling at low vapour qualities, i.e. vapour quality less than 0.15 at the exit. This was attributed to the dominance of single-phase liquid pressure drop in the channels at low vapour qualities. The liquid viscosity decreases at higher inlet temperatures, resulting in a higher single-phase pressure drop component and consequently higher channel pressure drop. Whilst the authors did not comment on the weak subcooling effect at higher vapour qualities, this is of course not expected at high exit qualities where the two-phase pressure drop component dominates.

On the contrary, Yin et al. [40] found a notable effect of subcooling on two-phase pressure drop only at low heat fluxes where bubbly and slug flow dominated in the channels. The authors reasoned that this is because decreasing inlet subcooling promoted nucleate boiling, which resulted in an increase in the frictional pressure drop in the channels. A combination of the shorter subcooled length and dominance of

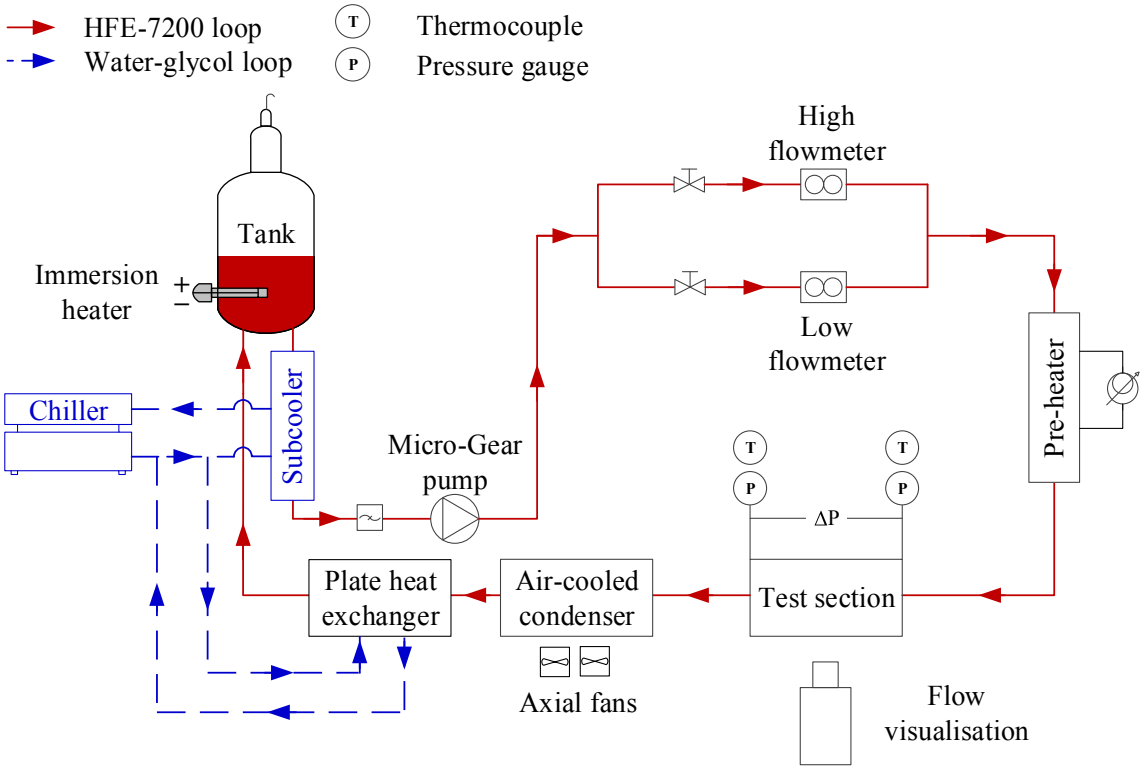

Fig. 1. Schematic of experimental facility.

stratified flow at higher heat flux conditions resulted in an insignificant subcooling effect in this region. Additionally, Zeng et al. [31] attributed higher heat sink pressure drop to more severe flow boiling instabilities when operating at higher inlet subcooling degrees. In summary, and as mentioned in the opening statement of this part on the effect of subcooling on two-phase pressure drop, there is evidence that the two-phase pressure drop decreases with increasing inlet subcooling. However, there are some reports to the contrary and this requires some further work.

Overall, the effects of inlet subcooling on flow boiling behaviour needs to be clarified and in general, there is a lack of literature on the effect of inlet subcooling on the flow boiling characteristics of HFE fluids. Moreover, very high degree of subcooling was employed in several studies such as in Chen et al. [27], where the subcooling degree was 70 K, as well as in Lee and Mudawar [11,44], where HFE-7100 at sub-atmospheric inlet temperatures of −30 °C was conveyed to the microchannel heat sink. Such low coolant temperatures may not be suitable for some compact and integrated cooling systems with limited space and energy consumption allocation to the integrated thermal unit. A two-stage cascade refrigeration system was used to condition water temperatures in the study of Lee and Mudawar [11,44]. Although CHF was enhanced up to 6.9 MW/m^2, the resultant thermal management solution would likely exceed size and weight constraints typically imposed the majority of cooling applications. In addition, most studies did not assess the effect of inlet subcooling on temperature uniformity on the heat sink, which was reported to worsen in Bogojevic et al. [34], and is also important in view of minimising thermal stresses on the chip die. In this paper, the effect of inlet subcooling on the heat transfer and pressure drop trend of dielectric fluid HFE-7200 in a copper microchannel heat sink is investigated. Flow boiling experiments at P = 1 bar, G = 200 kg/m^2 s and subcooling degrees of ΔT_{sub} = 5, 10 and 20 K are conducted for wall heat fluxes in the range of q_w'' = 25.9–180.7 kW/m^2.

2. Experimental methodology

2.1. Experimental facility

A schematic diagram of the experimental facility is shown in Fig. 1. The main flow loop uses working fluid HFE-7200. The auxiliary chiller loop, which uses a water-glycol mixture, is also included. The main loop consists of a reservoir, a subcooler, a gear pump (GJ-N23FF2S from Micropump®), two Coriolis mass flowmeters (OPTIMASS 3000 S01 for mass fluxes up to 300 kg/m^2 s and OPTIMASS 3000 S03 for mass fluxes more than 300 kg/m^{2}s from Krohne), a tube-in-tube pre-heater, the microchannel evaporator test section, an air-cooled condenser and a plate heat exchanger. The pressure in the tank is regulated using an immersion heater in the reservoir connected to a PID controller. The mass flow rate through the test section is controlled by means of a digital pump drive (ISMATEC Reglo ZS©) connected to the gear pump. Power input to the pre-heater (maximum power input 1500 W) and test section are varied using two separate variacs to control fluid inlet temperature and test section heat flux. Two axial fans (ARX FD2412-A3251G) are mounted on the condenser to provide ambient air cooling. The secondary side (cold side) of the plate heat exchanger is connected to the water-glycol loop to provide additional cooling to the working fluid (hot side) prior to its return to the reservoir. The water-glycol chiller is also used to control the fluid temperature upstream of the pump using the subcooler. All measuring instruments (i.e. thermocouples, pressure transducers and flow meters) were connected to a National Instruments Data Acquisition System (DAQ) and monitored using an in-house LabVIEW program on the computer. Data was acquired for a period of 90 s at a frequency of 1 kHz after steady-state conditions were achieved and the values were averaged for data reduction. Steady-state condition was defined when the temperature, pressure and mass flow rates do not vary by more than ± 0.2 g/s for

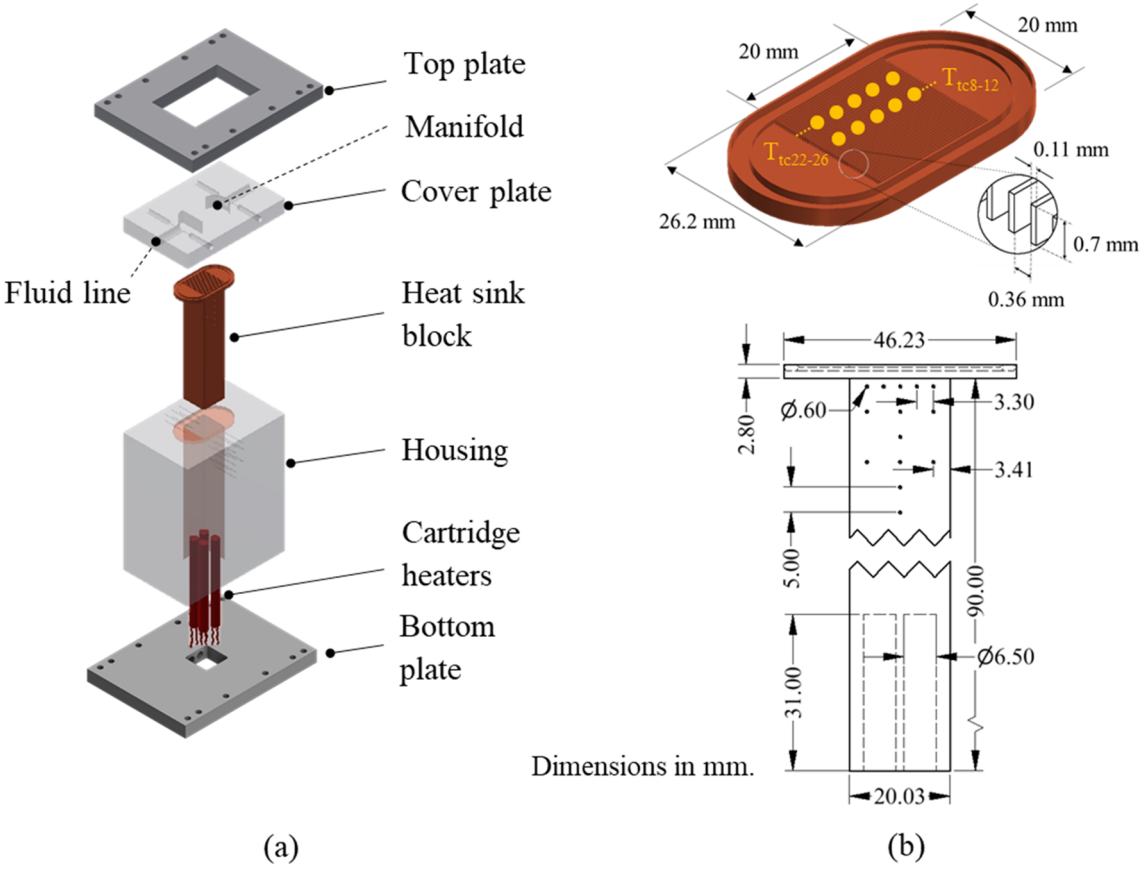

Fig. 2. Test section (a) Exploded view (b) Details of microchannel heat sink. The locations of wall temperature measurement are annotated.

mass flow rate, ± 0.5 K for inlet/outlet temperature and ± 0.05 bar for the inlet/outlet pressure over a period of at least 180 s. Live flow visualisation images were also used to assess steady flow phenomena before data acquisition.

The test section is shown in Fig. 2. It consists of an aluminium top plate, polycarbonate cover plate and housing, copper heat sink block, cartridge heaters and an aluminium bottom plate. The heat sink is made up of oxygen-free copper and has dimensions 90.0 mm (H) × 26.2 mm (W) × 46.2 mm (L), including the inlet and outlet plenum at the top of the block. Four cartridge heaters of maximum heating power 200 W each were inserted into vertical holes from the bottom of the block. Forty-four parallel microchannels were machined to a square base area of 20 mm × 20 mm using a high-precision milling machine (Kern HSPC-2216) with a carbide end-mill of 0.35 mm diameter at a speed of 18,000 rpm and a feed rate of 300 mm/min. The channel dimensions were 0.36 mm wide, 0.7 mm deep and 20 mm in length. The corresponding hydraulic diameter is D_h = 0.48 mm. The average surface roughness, R_a, was sampled at five different locations on the channel bottom wall using the Zygo NewView 500 surface profiler and was estimated to be around 0.23 μm.

Twenty-two K-type thermocouples were used to measure the temperature distribution in the heat sink block. Five thermocouples, each 3.3 mm apart, were positioned along the channel and inserted into the heat sink to a depth of 10 mm, i.e. to the centre of the block, and 1.6 mm from the channel bottom wall to measure axial temperature. The most upstream and downstream thermocouples are 3.4 mm from the channel inlet and outlet respectively. On the other side of the heat sink, five thermocouples were inserted at the same coordinates but only to a depth of 5 mm, i.e. to the quarter plane of the block, to measure traverse temperature distribution. Six thermocouples in the vertical direction, each 5 mm apart and starting from 1.6 mm from the bottom of the channel wall, were used to measure the temperature gradient along the height of the block. The inlet/outlet manifolds are machined in the polycarbonate top plate. The inlet and outlet pressure were measured at the inlet and outlet manifold respectively using two Omega™ PXM409-007BAI pressure transducers. The inlet and outlet fluid temperature were also measured at these points using two K-type thermocouples. Lastly, the total pressure drop across the heat sink (i.e. across the inlet and outlet manifold) is measured using an Omega™ PX409-015DWUI differential pressure transducer.

A high-speed camera (Phantom Miro Lab110) was coupled with a Huvitz HSZ-645TR microscope and LED lighting system for flow visualisation, operating at 5000 frames/s and at a resolution of 512 × 512 pixels. Flow visualisation was conducted at four locations along the channel array to capture flow pattern evolution corresponding to each experimental condition. High-speed recordings were conducted at 5000 fps at a magnification of 4.5x and a resolution of 512 × 512 pixels for a duration of 1.3 s at each location, see Fig. 3. It is important to note that the high-speed recordings are not simultaneous. Flow visualisation was conducted when all readings on LabVIEW appear to be at steady-state condition, i.e. as mentioned above, no significant changes in temperature, pressure and flow rate for at least a window of 180 s and the flow pattern is observed to be quasi-steady. Hence the flow patterns captured remain a good representation of the flow pattern development along the channels, although not simultaneously at each location. This was also verified by repeating the observations on at least two different occasions.

2.2. Data reduction

For single-phase validation, the experimental Fanning friction factor, f, is found by the following relation:

$$f = \frac{\Delta P_{ch} D_h \rho_f}{2 L_{ch} G_{ch}^2} \quad (1)$$

The pressure drop across the microchannel array, ΔP_{ch}, is given by:

$$\Delta P_{ch} = \Delta P_{total} - \Delta P_{ip} + \Delta P_{sc} + \Delta P_{se} + \Delta P_{op} \quad (2)$$

where ΔP_{total} is the total measured pressure drop. ΔP_{ip} and ΔP_{op} are the pressure drop components in the inlet and outlet plenum respectively, given in Eqs. (3) and (4). These include the pressure losses due to sudden expansion from the fluid line (fluid line radius, R_{fl} = 3 mm) at the inlet manifold, sudden contraction into the fluid line at the outlet manifold and 90° bend in both manifolds (plenum radius, R_p = 9.7 mm), calculated based on the method detailed in Remsburg [45].

$$\Delta P_{ip} = \frac{1}{2}\rho_f \left\{ V_p^2 K_{90} + V_{fl}^2 \left[\alpha_p^2 - 1 + \left(1 - \frac{1}{\alpha_p}\right)^2 \right] \right\} \quad (3)$$

$$\Delta P_{op} = \frac{1}{2}\rho_f \left\{ V_p^2 K_{90} + V_{fl}^2 \left[1 - \frac{1}{\alpha_p^2} + \frac{1}{2}\left(1 - \frac{1}{\alpha_p}\right) \right] \right\} \quad (4)$$

The coefficient of pressure loss through a 90° bend, K_{90}, is given as 1.2 in Phillips (1987) [46]. The plenum area ratio, $\hat{1} \pm_p$, is defined as the area of the plenum over the cross-sectional area of the fluid line. In the current test section, α_p = 150 mm.

The pressure drop components due to sudden contraction into the microchannels and sudden expansion from the microchannels are ΔP_{sc} and ΔP_{se} respectively, where V_{ch} and β are the fluid velocity in the microchannel array and the microchannel area ratio respectively.

$$\Delta P_{sc} = \frac{1}{2}\rho_f V_{ch}^2 \left[1 - \beta^2 + \frac{1}{2}(1 - \beta^2) \right] \quad (5)$$

$$\Delta P_{se} = \frac{1}{2}\rho_f V_{ch}^2 \left[\frac{1}{\beta^2} - 1 + (1 - \beta)^2 \right] \quad (6)$$

The area ratio β is the area flow area of the microchannels over the frontal area of the channel array, i.e. $\beta = (NW_{ch}H_{ch})/(H_{ch}W)$. W is the width of the heat sink, W = 20 mm, and for the present channel configuration, β = 0.78. Lastly, $P_{i,ch}$ is the pressure at the inlet of the channel array, corrected for pressure losses in the inlet manifold, i.e. $P_{i,ch} = P_i - P_{ip} - P_{sc}$.

The average single-phase Nusselt number is defined in Eq. (7), where k_f is the liquid thermal conductivity:

$$\bar{Nu} = \frac{1}{L_{ch}} \int_{L=0}^{L=L_{ch}} \frac{h_{sp(z)} D_h}{k_f} \, dz \quad (7)$$

The local heat transfer coefficient, $h_{(z)}$, including both the local heat transfer coefficient in the single-phase, $h_{sp(z)}$ and two-phase region, $h_{tp(z)}$, are obtained at thermocouple locations along the channel bottom wall, i.e. dimensionless locations z/L = 0.17, 0.34, 0.5, 0.67 and 0.83 as follows:

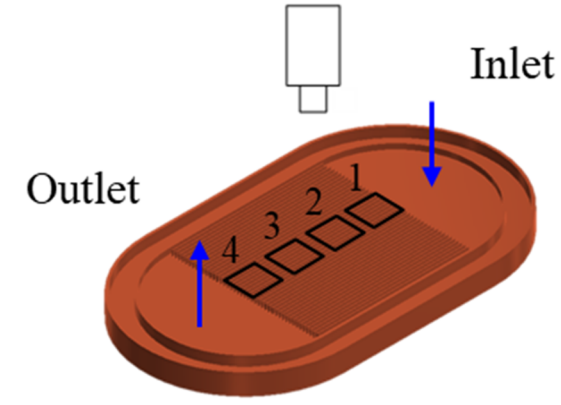

Fig. 3. Camera locations for flow visualisation along the channel. Each location has a length of approximately 4.4 mm in the direction of the flow and a width of approximately 4.4 mm. Location 1 starts at the channel inlet.

$$h_{(z)} = \frac{q_b''(W_{ch} + W_f)}{(T_{w(z)} - T_{f(z)})(W_{ch} + 2\eta H_{ch})} \quad (8)$$

The fin efficiency, η and fin parameter, m, are found iteratively using the formula given in Incropera et al. [47] in Eqs. (9) and (10).

$$\eta = \frac{\tanh(mH_{ch})}{mH_{ch}} \quad (9)$$

$$m = \sqrt{\frac{2h_{(z)}}{k_{cu}W_{fin}}} \quad (10)$$

The local wall temperature, $T_{w(z)}$, is extrapolated from the axial thermocouple measurements along the channel, $T_{tc(z)}$, based on energy balance.

$$T_{w(z)} = T_{tc(z)} - \frac{q_b''Y}{k_{cu}} \quad (11)$$

$$q_b'' = k_{cu}\frac{dT}{dy}\bigg|_{y=0} \quad (12)$$

where q_b'' is the base heat flux calculated from the vertical temperature gradient on the copper block (see Eq. (12)) and Y is the distance between the bottom wall of the channel and the topmost thermocouple, i.e. 1.6 mm. k_{cu} is the thermal conductivity of the copper block.

The bulk fluid temperature, $T_{f(z)}$ is calculated based on Eq. (13) if in the single-phase region or evaluated at the local saturation pressure, $P_{sat(z)}$, if the corresponding z location is in the flow boiling region, see below.

$$T_{f(z)} = T_i + \frac{q_b''Wz}{\dot{m}c_{p,f}} \quad (13)$$

where $P_{sat(z)}$ is calculated with the assumption of a linear pressure drop in the channels as follows:

$$P_{sat(z)} = P_{sat(z,sub)} - \left(\frac{z - L_{sub}}{L_{ch} - L_{sub}}\right)\Delta P_{tp} \quad (14)$$

In this study, a linear pressure drop assumption was used as an approximation as local pressure measurements were not available. Additionally, the adoption of a parabolic pressure drop trend using two-phase pressure drop models [48,49] generally resulted in an over-prediction of pressure drop at the outlet of the heat sink, which could lead to an over-prediction of local heat transfer coefficients near the outlet of the channel array.

In Eq. (14), L_{sub} and L_{ch} are the subcooled length and channel length respectively, while ΔP_{tp} is the two-phase pressure drop in the channels. The local saturation pressure at the location of zero quality, $P_{sat(z,sub)}$ is given as:

$$P_{sat(z,sub)} = P_{i,ch} - \frac{2f_{app}G_{ch}^2L_{sub}}{D_h\rho_f} \quad (15)$$

where f_{app} is the apparent friction factor, evaluated using the relation proposed by Shah and London [50] for developing flows:

$$f_{app} = \frac{1}{Re}\left[\frac{3.44}{\sqrt{L_{sub}^+}} + \frac{(fRe)_{fd} + \frac{K(\infty)}{4L_{sub}^+} - \frac{3.44}{\sqrt{L_{sub}^+}}}{1 + \frac{C^+}{(L_{sub}^+)^2}}\right] \quad (16)$$

The fully-developed Poiseuille number, $(fRe)_{fd}$, and constants $K(\infty)$ and C^+ are given as 15.46, 0.97 and 0.00029 respectively for the nominal channel dimensions in this study [50]. The dimensionless subcooled length, L_{sub}^+, is determined by $L_{sub}/(ReD_h)$. L_{sub} is derived iteratively based on Eqs. (15) and (17).

$$L_{sub} = \frac{\dot{m}c_{p,f}(T_{sat(z,sub)} - T_i)}{q_b''W} \quad (17)$$

In Eq. (17), $T_{sat(z,sub)}$ is the saturation temperature at the location of zero quality, to be evaluated at $P_{sat(z,sub)}$. An initial value for $T_{sat(z,sub)}$ is assumed and L_{sub} is calculated. The value is substituted into Eq. (15) to obtain an estimate of $P_{sat(z,sub)}$. The saturation temperature evaluated at the estimated $P_{sat(z,sub)}$ is compared against the initial value assumed for $T_{sat(z,sub)}$. The iteration is continued until the assumed temperature matches the estimated temperature within an error margin of ± 0.001 K.

The two-phase pressure drop in the channels, ΔP_{tp}, is obtained by the following relation:

$$\Delta P_{tp} = \Delta P_{ch} - \Delta P_{sp} \quad (18)$$

The single-phase pressure drop, ΔP_{sp} is the pressure drop in the subcooled region and is calculated based on the single-phase friction factor, f_{sp}, evaluated using the relation proposed by Shah and London [50] for developing flows in Eq. (16).

$$\Delta P_{sp} = \frac{G_{ch}^2 f_{sp} L_{sub}\rho_f}{2D_h} \quad (19)$$

The local and exit vapour quality (i.e. z = 20 mm) is calculated based on energy balance:

$$x_{(z)} = \frac{i_{(z)} - i_{f(z)}}{i_{fg(z)}} \quad (20)$$

$$i_{(z)} = i_i + \frac{q_b''Wz}{\dot{m}} \quad (21)$$

If the exit vapour quality is larger than zero, i.e. two-phase flow at the outlet of the heat sink, the procedure to calculate pressure drop is as described above, with the exception of the pressure losses in the outlet plenum, $\Delta P_{op,tp}$ and $\Delta P_{se,tp}$ are estimated based on the two-phase pressure drop equations given in Collier and Thome [51] instead. $\Delta P_{op,tp}$ consists of two components, namely the two-phase pressure drop through a bend, $\Delta P_{bd,tp}$, and the two-phase pressure loss due to sudden contraction into the fluid line, $\Delta P_{sc,fl,tp}$.

$$\Delta P_{op,tp} = \Delta P_{bd,tp} + \Delta P_{sc,fl,tp} \quad (22)$$

where $\Delta P_{bd,tp}$ is calculated based on the method proposed by Chisholm [52], where B is a constant given in Eq. (24), R_{bd} is the bend radius of the plenum (5 mm) and D_p is the diameter of the plenum (19.4 mm).

$$\Delta P_{bd,tp} = \left\{\frac{G_{ch}^2 v_f K_{90}}{2}\right\} * \left\{1 + \left[\left(\frac{\rho_f}{\rho_g} - 1\right) * (Bx_e(1 - x_e) + x_e^2)\right]\right\} \quad (23)$$

$$B = 1 + \frac{2.2}{K_{90}\left(2 + \frac{R_{bd}}{D_p}\right)} \quad (24)$$

On the other hand, $\Delta P_{sc,fl,tp}$ is calculated based on the equation derived in Collier and Thome [51], where the constant C_c is 0.635 for the current plenum area ratio, based on the relation proposed by Chisholm [53].

$$\Delta P_{sc,fl,tp} = \frac{G_{ch}^2}{2\rho_f}\left[\left(\frac{1}{C_c} - 1\right)^2 + \left(1 - \frac{1}{\alpha_p^2}\right)\right] * \left(1 + \frac{\rho_f}{\rho_g}\right)x_e \quad (25)$$

The two-phase pressure drop due to sudden expansion from the microchannel array may be calculated as follows [51]:

$$\Delta P_{se,tp} = \frac{G_{ch}^2}{\rho_f}\left[\frac{1}{\beta}\left(1 - \frac{1}{\beta}\right)\right] * \left[\frac{(1 - x_e)^2}{(1 - \alpha_v)} + \left(\frac{\rho_f}{\rho_g}\frac{x_e^2}{\alpha_v}\right)\right] \quad (26)$$

where the void fraction, α_v, is estimated using the correlation developed by Kawahara et al. [54].

$$\alpha_v = \frac{0.03\left(\frac{J_{g(z)}}{J_{g(z)} + J_{l(z)}}\right)^{0.5}}{1 - 0.97\left(\frac{J_{g(z)}}{J_{g(z)} + J_{l(z)}}\right)^{0.5}} \quad (27)$$

The liquid and vapour superficial velocities, $J_{l(z)}$ and $J_{g(z)}$, are given in Eqs. (28) and (29) respectively.

$$J_{l(z)} = \frac{G_{ch}(1 - x_z)}{\rho_f} \quad (28)$$

$$J_{g(z)} = \frac{G_{ch} x_z}{\rho_g} \quad (29)$$

The overall heat transfer coefficient, $\bar{h}_{(z)}$, is calculated based on all five axial heat transfer measurements with respect to the *total channel length*, i.e. includes also the heat transfer coefficients in the subcooled region, where applicable.

$$\bar{h}_{(z)} = \frac{1}{L_{ch}} \int_{L=0}^{L=L_{ch}} h_{(z)}\, dz \quad (30)$$

As covered above, $h_{(z)}$ is calculated based on Eq. (8). The average two-phase heat transfer coefficient, $\bar{h}_{tp(z)}$, is obtained across the saturated boiling region:

$$\bar{h}_{tp(z)} = \frac{1}{L_{ch} - L_{sub}} \int_{L=L_{sub}}^{L=L_{ch}} h_{(z)}\, dz \quad (31)$$

To ensure comparability with other flow boiling studies employing different heat sink configurations, heat transfer coefficients are presented as a function of wall heat flux, q_w''.

$$q_w'' = \frac{q_b''(W_{ch} + W_{fin})}{(W_{ch} + 2H_{ch})} \quad (32)$$

All thermophysical properties of HFE-7200 were obtained from Engineering Equation Solver (EES).

The working fluid, 3M™ Novec™ HFE-7200, was selected for its high dielectric strength (minimises damage in the case of coolant leakage), low ozone depletion potential (ODP) and low global warming potential (GWP). The relevant fluid properties of the working fluid at P = 1 bar are presented in Table 1.

To ensure reproducibility in the experimental results, degassing procedures were conducted prior to experiments in this study. The working fluid was boiled vigorously for at least an hour and degassed air is released through a degassing tap at the top of the reservoir. This process is repeated until the measured temperature and pressure in the tank corresponds to the saturation conditions of pure HFE-7200. The measurement and propagated experimental uncertainties, the latter evaluated using the method described in Coleman and Steele [55], are listed in Table 2. The uncertainty of the thermocouple was obtained using a calibration procedure with a precision thermometer (ASL F250 MK II) in a constant temperature bath using a water-glycol mixture.

Flow boiling experiments were conducted at a mass flux and inlet pressure condition of G = 200 kg/m^2 s and P = 1 bar. At this pressure the fluid saturation temperature is 75.1 °C. The degree of inlet subcooling was varied from ΔT_{sub} = 5 K, 10 K and to 20 K, corresponding to approximate inlet temperatures of T_i = 70 °C, 65 °C and 55 °C. The range of wall heat fluxes investigated is between q_w'' = 25.8 to 180.7 kW/m^2. The equivalent base heat flux values for the microchannel heat sink with a 20 mm × 20 mm footprint area is q_b'' = 99.1–605.3 kW/m^2.

3. Results

3.1. Single-phase validation

Single-phase experiments were conducted to validate the measurement instruments and the experimental setup. Figs. 4 and 5 show the single-phase experimental friction factor and average single-phase

Table 2
Experimental uncertainties.

Equipment/Parameter	Uncertainty
K-type thermocouple	± 0.2 K
Inlet/outlet pressure transducer	± 0.08%
Total pressure drop	± 0.08%
Mass flow rate	± 0.035%
Channel mass flux	± 0.63%
Fanning friction factor	± 2.39–2.46%
Average Nusselt number	± 5.57–11.71%
Local heat transfer coefficient	± 3.73–8.82%
Local vapour quality	± 2.02–12.87%
Heat flux	± 1.94–4.36%

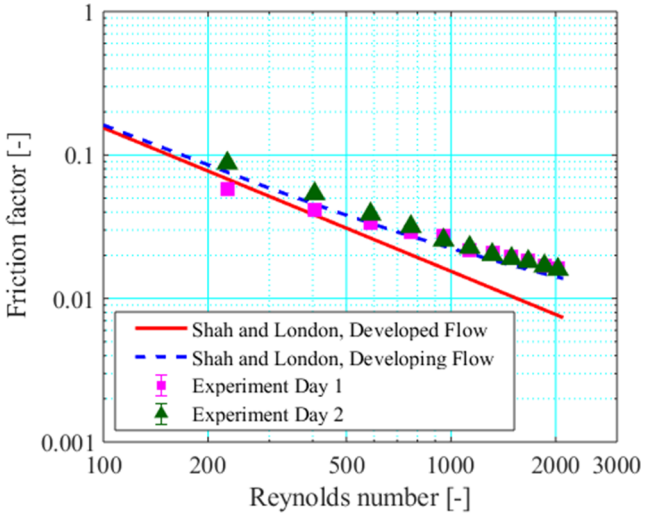

Fig. 4. Experimental single-phase friction factor vs. Reynolds number. Error bars are between ± 2.39–2.46% but are too small to be visible in the figure.

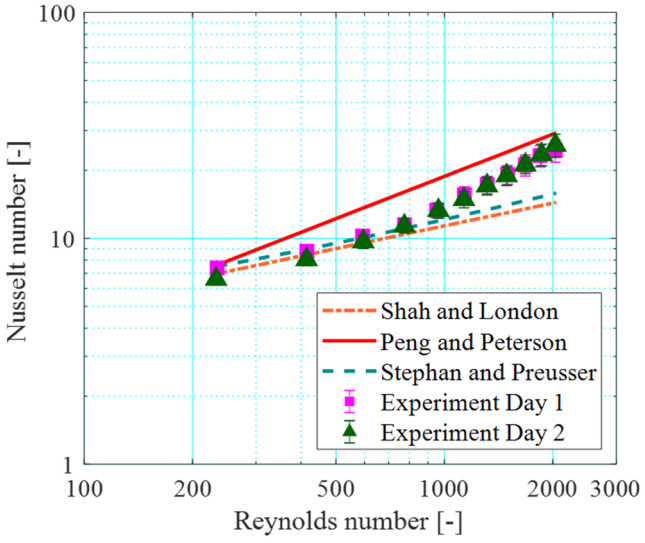

Fig. 5. Experimental single-phase Nusselt number vs. Reynolds number.

Table 1
Properties of fluid HFE-7200 at P = 1 bar.

P_{sat} [bar]	T_{sat} [°C]	c_p [J/kg K]	i_{fg} [kJ/kg]	ρ_f [kg/m^3]	ρ_g [kg/m^3]	μ_f [kPa s]	μ_g [kPa s]	σ [mN/m]
1.0	75.1	1086	110	1303	9.7	0.36	0.012	9.6

Nusselt number with respect to Reynolds number.

The experimental single-phase friction factor is in good agreement with the correlations given in Shah and London [50], proposed for developing and fully developed laminar flows in non-circular horizontal ducts. The average Nusselt number obtained in single-phase heat transfer experiments were well predicted by established correlations for laminar flows in microchannels, namely the Shah and London [50], Peng and Peterson [56] and Stephan and Preusser [57]. The figures also show good repeatability of single-phase experiments in this study.

3.2. Flow boiling results

3.2.1. Effect on reproducibility

Flow boiling experiments were conducted to investigate the effect of inlet subcooling, namely at ΔT_{sub} = 5 K, 10 K and 20 K for wall heat fluxes ranging from q_w'' = 25.9 kW/m^2 to 180.7 kW/m^2. This corresponds to vapour qualities from 0 to 1 at the exit of the microchannel heat sink. The channel mass flux and inlet pressure were kept constant at G = 200 kg/m^2 s and P = 1 bar in order to isolate the effect of inlet subcooling on microchannel flow boiling behaviour.

The saturation temperature of HFE-7200 at P = 1 bar is 75.1 °C, as summarised in Table 1. The mean absolute deviation, MAE, may be used to further assess the repeatability of experiments:

$$MAE = \frac{1}{n}\sum \left| \frac{j_{day1} - j_{day2}}{j_{day1}} \right| \times 100\% \quad (33)$$

where j is the experimental parameter and n is the number of data points collected, can be used here to compare the two data sets.

Notably, experiments at ΔT_{sub} = 10 K and 20 K were more repeatable in comparison to the experiments conducted at inlet subcooling conditions of ΔT_{sub} = 5 K, see Figs. 6 and 7. The MAE of experiments at the higher subcooling conditions of 10 K and 20 K were ± 2.9% and ± 3.8% respectively, while the mean average deviation was up to ± 12.3% at ΔT_{sub} = 5 K. The deviation in the data were also slightly higher at lower heat fluxes in the channel. This could be related to flow reversal in the channel due to slug growth following the onset of boiling and potential upstream compressibility effects in the channel, which could also affect heat transfer characteristics in microchannels [58,59]. The experiments at the highest inlet temperature was only conducted at the lowest mass flux condition of G = 200 kg/m^2 s. Flow reversal and hence possible effects on reproducibility is expected to be less at higher mass fluxes. This was the case when mass flux was increased to G = 300 and 400 kg/m^2 s. Similar results were observed in Al-Zaidi [60] for reproducibility comparisons at higher mass fluxes.

3.2.2. Effect on flow patterns

Flow patterns developed sequentially from bubbly to slug, churn and annular flow in the channels at all subcooling conditions. Flow regime transition boundaries were delayed to higher vapour quality values at higher inlet subcooling conditions (i.e. lower inlet temperature). This agrees with the observations of Chen et al. [27] and Zeng et al. [31]. At a given wall heat flux condition of q_w'' ~ 107 kW/m^2, flow patterns monitored at the channel inlet (camera location 1, see Fig. 3) changed from churn to slug and bubbly flow with increasing subcooling, as shown in Fig. 8. Accordingly, the vapour quality at which flow regime transitions were observed are summarised in Table 3. The quality for transition from bubbly to slug flow, as well as from churn to annular flow, increased gradually with subcooling. Between ΔT_{sub} = 5 K and ΔT_{sub} = 10 K, only a small shift in the slug-churn transition boundary was observed in the heat sink. However, this change was more evident as ΔT_{sub} increased to 20 K. In the subcooled region of the channels, the liquid layer directly adjacent to the heated channel walls may still become superheated, even when the bulk liquid temperature is below saturation. Bubbles were captured to nucleate from the channel side walls, but shrink and eventually re-condense into the bulk flow soon after departure, as illustrated in Fig. 9.

Consequently, the potential for bubble coalescence in the channels is lower at higher inlet subcooling conditions due to bubble shrinkage in the subcooled region at higher subcooling, hence delaying the transition from bubbly to slug flow in the channels. Additionally, increasing the inlet subcooling degree effectively extends the subcooled region in the channels. From Fig. 10, it is clear that the subcooled length decreases with heat flux but increases with inlet subcooling at a given wall heat flux condition. As a result, transition from bubbly to slug flow occurred at higher vapour qualities in the heat sink at higher inlet subcooling conditions, since the bubble coalescence phenomenon, which triggers flow regime transition from bubbly to slug flow, was less vigorous in the subcooled region of the channels. Similarly, the subsequent flow regime transition boundaries were affected, i.e. slug-churn and churn-annular transition were also delayed to higher vapour qualities at higher inlet subcooling conditions.

The model proposed by Hsu [21], given in Eq. (34), was applied to predict the range of nucleation sites at inlet subcooling conditions of ΔT_{sub} = 5 K, 10 K and 20 K. This is shown in Fig. 11.

$$r_{c(max,min)} = \frac{\delta_t}{4}\frac{\Delta T_{sup}}{(\Delta T_{sup} + \Delta T_{sub})}\left[1 \pm \sqrt{1 - \frac{12.8\sigma T_{sat}(\Delta T_{sup} + \Delta T_{sub})}{\delta_t \rho_g i_{fg} \Delta T_{sup}^2}}\right] \quad (34)$$

The parameters δ_t and ΔT_{sup} are the thickness of the thermal boundary layer and the degree of wall superheat. δ_t is estimated using $\delta_t = k_f / h_{sp}$, where the single-phase liquid heat transfer coefficient, h_{sp}, is calculated based on the fully-developed laminar flow equation (Nu = 4.36), see [19] for more information on this work.

From Fig. 11, for a given degree of wall superheat, the range of nucleation sites narrow with increasing degree of subcooling. Cavities with radii larger than 10 μm are significantly affected by the subcooling degree, while the nucleation activity from small cavities are less sensitive to changes in system subcooling, for the range of subcooling investigated in the current study. The less vigorous bubble nucleation activity (lower bubble generation frequency) at higher subcooling conditions could also have contributed to the delay in flow pattern transition, owing to less bubble coagulation in the channels. Lower bubble generation frequencies at higher subcooling conditions were also suggested by Euh et al. [23] and Goel et al. [24] for macroscale boiling.

The response of different fluids to changes in the degree of subcooling is expected to vary since the bubble generation frequency and

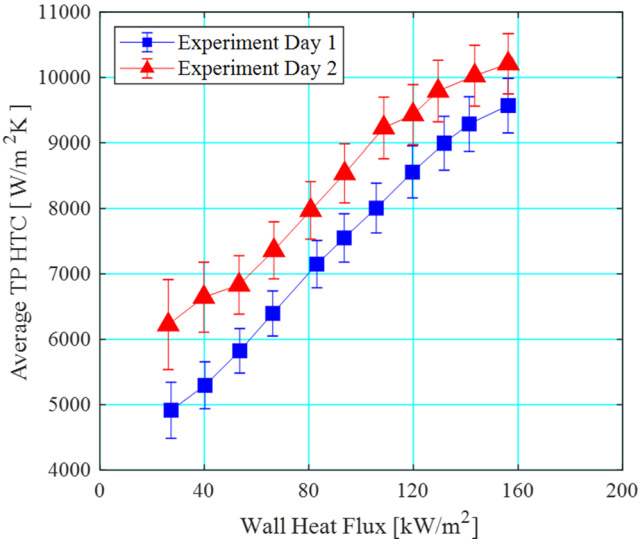

Fig. 6. Repeatability of experiments at P = 1 bar, G = 200 kg/m^2 s and ΔT_{sub} = 5 K. The mean average deviation of the experimental data is ± 12.3%.

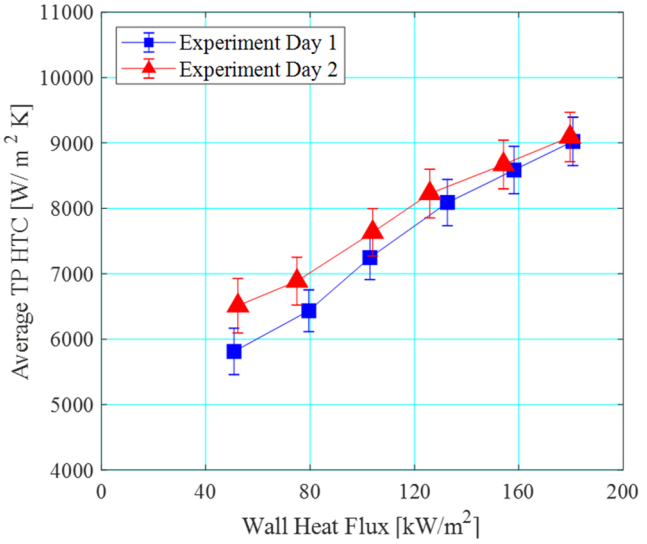

Fig. 7. Repeatability of experiments at P = 1 bar, G = 200 kg/m^2 s and ΔT_{sub} = 20 K. The mean average deviation of the experimental data is ± 3.8%.

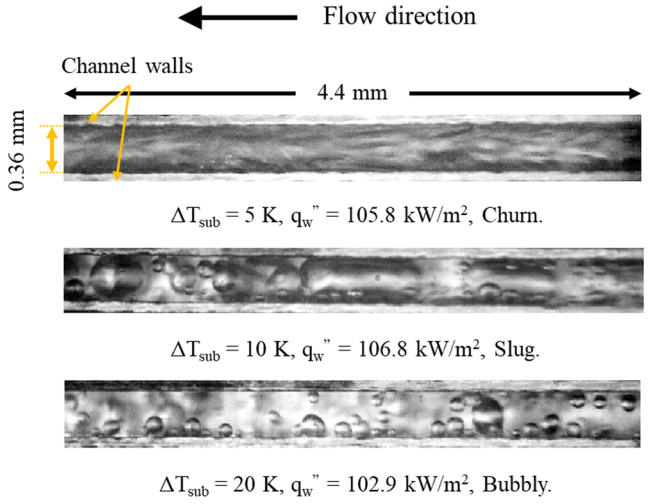

Fig. 8. Flow patterns observed at camera location 1 (channel inlet, see Fig. 3), at three inlet subcooling conditions for G = 200 kg/m^2 s and an approximate wall heat flux of $q_w^{"} \sim 107$ kW/m^2.

Table 3
Flow pattern transition vapour qualities at P = 1 bar and G = 200 kg/m^2 s for wall heat fluxes ranging from $q_w^{"}$ = 25.9 – 180.7 kW/m^2.

ΔT_{sub} [K]	$x_{B\text{-}S}$ [–]	$x_{S\text{-}C}$ [–]	$x_{C\text{-}A}$ [–]
5	0.012	0.064	0.23
10	0.037	0.068	0.30
20	0.049	0.125	0.34

$x_{B\text{-}S}$ = transition from bubbly to slug flow.
$x_{S\text{-}C}$ = transition from slug to churn flow.
$x_{C\text{-}A}$ = transition from churn to annular flow.

departure diameter will be different. This is true even for similar-use fluids, see [19]. For example, the bubble generation frequency of fluid R245fa is much higher than that of R134a. It is therefore expected that slug or churn flow will be observed soon after boiling incipience for R245fa and thus the flow patterns maybe less affected by the degree of subcooling. Water has a much higher bubble generation frequency and therefore this may affect the extent of the influence of the degree of subcooling even more. This topic is certainly worth investigating further for a conclusion.

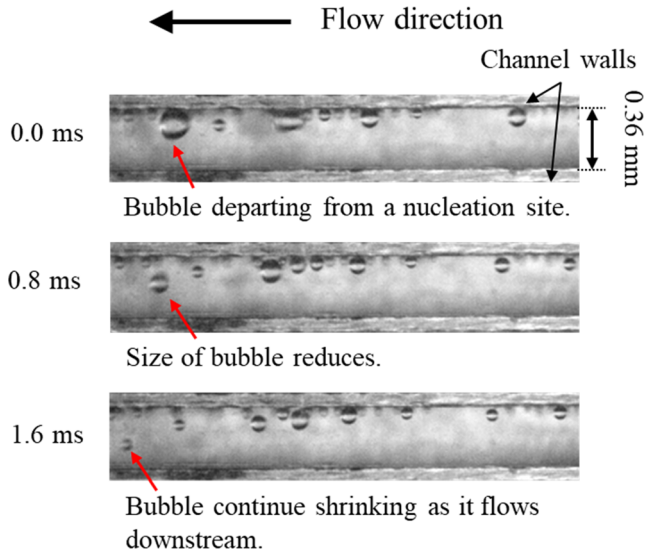

Fig. 9. Bubble shrinkage in subcooled liquid. Images shown were captured at location 1 (see Fig. 3), under conditions P = 1 bar, G = 200 kg/m^2 s, $q_w^{"}$ = 25.9 kW/m^2 and ΔT_{sub} = 20 K.

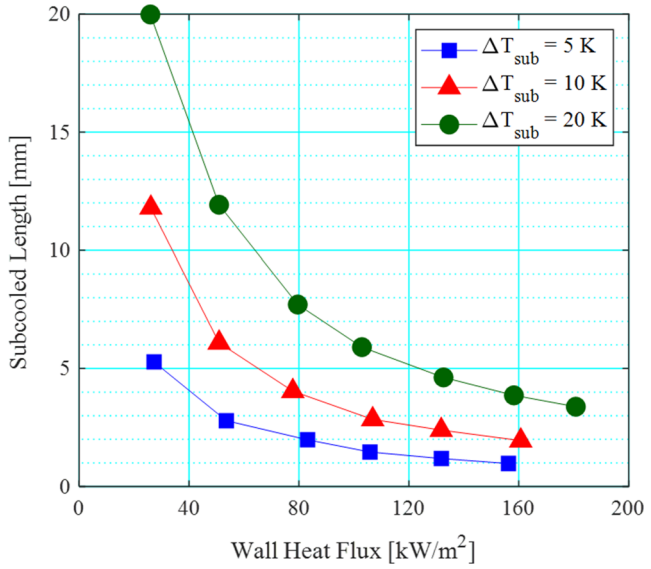

Fig. 10. Subcooled length as a function of wall heat flux for inlet subcooling ΔT_{sub} = 5 K, 10 K and 20 K at P = 1 bar and G = 200 kg/m^2 s.

3.2.3. *Effect on two-phase instability*

The standard deviation of the measured pressure drop signal across the heat sink is presented in Fig. 12(a) and (b) for $q_w^{"} \sim 51$ kW/m^2 and $q_w^{"} \sim 132$ kW/m^2 respectively in order to assess the effect of inlet subcooling on flow boiling instabilities in the microchannel heat sink. The standard deviation is calculated as follows:

$$\sigma(\Delta j) = \sqrt{\frac{\sum_{n=1}^{n} (j_n - \bar{j}\, n)^2}{n}} \quad (35)$$

where j is the experimental parameter and n is the number of data points.

Pressure drop oscillations were attributed to alternating vapour flow into the inlet plenum and the incoming subcooled liquid in Bogojevic et al. [34]. In Kingston et al. [36], fluctuations in the pressure drop, temperature and mass flux signals were correlated to periodic

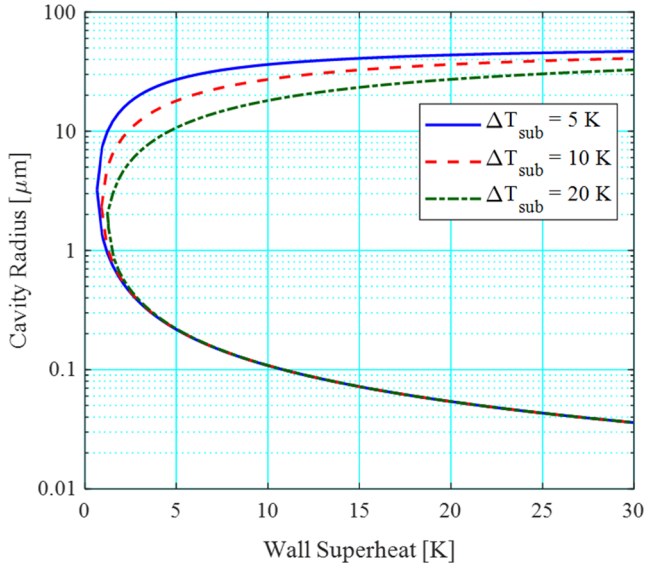

Fig. 11. Range of active nucleation cavity radii as a function of wall superheat at subcooling conditions of ΔT_{sub} = 5, 10 and 20 K, as predicted using Hsu's model [21].

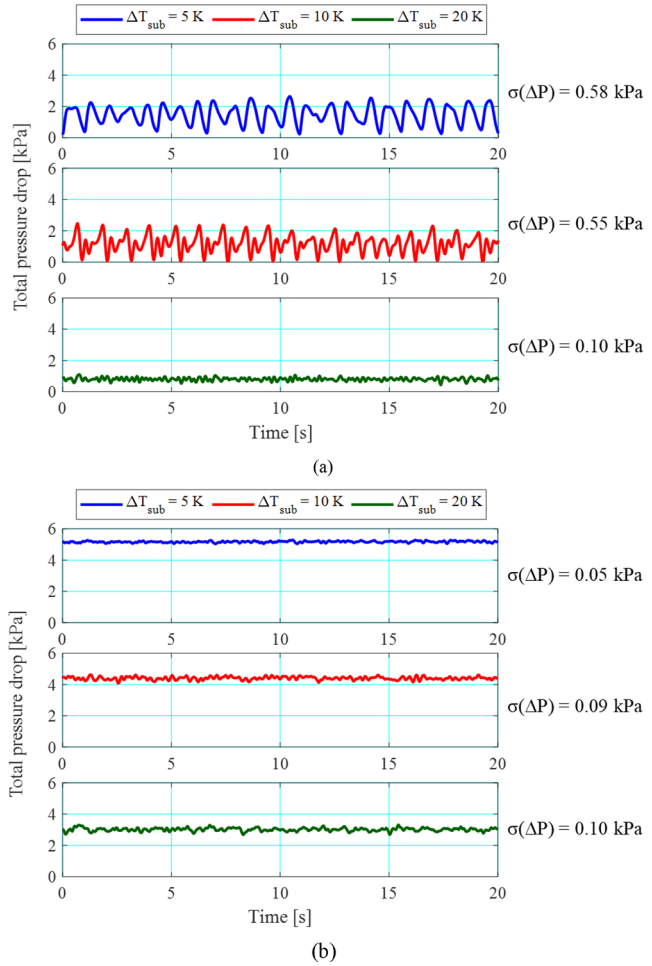

Fig. 12. Measured pressure drop across the heat sink at (a) $q_w^{"} \sim 51$ kW/m^2 and (b) $q_w^{"} \sim 132$ kW/m^2 over a window of 20 s for G = 200 kg/m^2 s and inlet subcooling conditions 5, 10 and 20 K.

occurrences of rapid bubble growth and confined bubble expansion in the channel array.

Pressure drop oscillations observed in the current study may be associated with flow reversal triggered by the expansion of vapour slugs in the channels, which is frequently observed with the presence of confined slugs. Flow reversal captured at the inlet of the heat sink showed a typical cycle of flow reversal to be between 350 ms and 600 ms long. An example of flow reversal captured at P = 1 bar, G = 300 kg/m^2 s, $q_w^{"}$ = 24.8 kW/m^2 and ΔT_{sub} = 10 K is illustrated in Fig. 13. Due to limitations in camera memory, flow visualisation at extended time periods of 6.5 s at the inlet plenum (normal flow pattern visualisation along the channel are only for a duration of 1.3 s) were only conducted at select operating conditions to monitor the full occurrence of flow reversal phenomenon in this study. While the flow conditions in Fig. 13 do not directly correspond to the range of operating conditions presented in the current study, they are a good representation of the type of flow reversal observed in the heat sink at low heat fluxes. This is confirmed through the observation of flow patterns captured along the channels at different mass fluxes, including G = 200 kg/m^2 s of the present range, for various heat flux conditions.

The peak in pressure drop readings may be associated with upstream pressurisation due to vapour expansion in the upstream direction (see Fig. 13(b)–(c)). As the slugs grow to the full length of the channels, the flow resistance is reduced and results in a drop in measured pressure drop across the heat sink. This corresponds to the pressure drop instability phenomenon observed in Kingston et al. [36] during confined bubble expansion. In order to capture these occurrences, the response time of the measuring instrument must be shorter than the time period of the flow phenomenon. Based on the manufacturer's specification, the response time of the differential pressure transducer is less than 1 ms [61], hence the instrumentation was suitable for capturing the pressure oscillations. The response time of the 0.5 mm diameter K-type thermocouple used to measure fluid inlet temperature is given as 0.03 s [62]. In order to obtain a meaningful measurement of the dynamic temperature behaviour corresponding to flow reversal in the microchannels, temperature measurement techniques such as temperature sensors [34] that allows for higher response rates should be employed. Hence only the signal obtained from the differential pressure transducer will be used in the discussions on flow boiling instabilities in the current study.

At low heat flux, increasing inlet subcooling, particularly to 20 K, reduced pressure oscillations in the heat sink. The standard deviation of the measured pressure drop signal at 5 K was 0.58 kPa. Increasing inlet subcooling mitigated pressure drop oscillations to 0.1 kPa at 20 K, see Fig. 12(a). This could be due to the delayed development of slug flow due to less intensive bubble coalescence phenomenon in the channels at higher subcooling for a given wall heat flux condition. At $q_w^{"} \sim 51$ kW/m^2, the slug flow regime was observed near the inlet of the heat sink at 5 K and 10 K, while bubbly flow was largely observed in the heat sink at 20 K. As mentioned above, the expansion of vapour slugs in the channels trigger vapour backflow into the inlet plenum, and is believed to contribute to the larger pressure drop oscillations observed at lower inlet subcooling. Kingston et al. [36] also found that increasing inlet subcooling at a given wall heat flux condition delayed the onset of pressure drop instabilities in their parallel microchannel heat sink using fluid HFE-7100.

The magnitude of two-phase oscillations stabilised in the churn and annular flow regime, evident by comparing the signals illustrated in Fig. 12(a) and (b). This could be due to the presence of a stable vapour core in the annular flow regime, which could have resulted in lower flow resistance in the channels, lower upstream compressibility and thus less severe vapour backflow to the inlet plenum of the heat sink. However, increasing inlet subcooling at wall heat fluxes where the annular flow regime is dominant increased the pressure fluctuations slightly. The standard deviation of the measured heat sink pressure drop increased from 0.05 kPa at 5 K to 0.1 kPa at 20 K. This agrees with

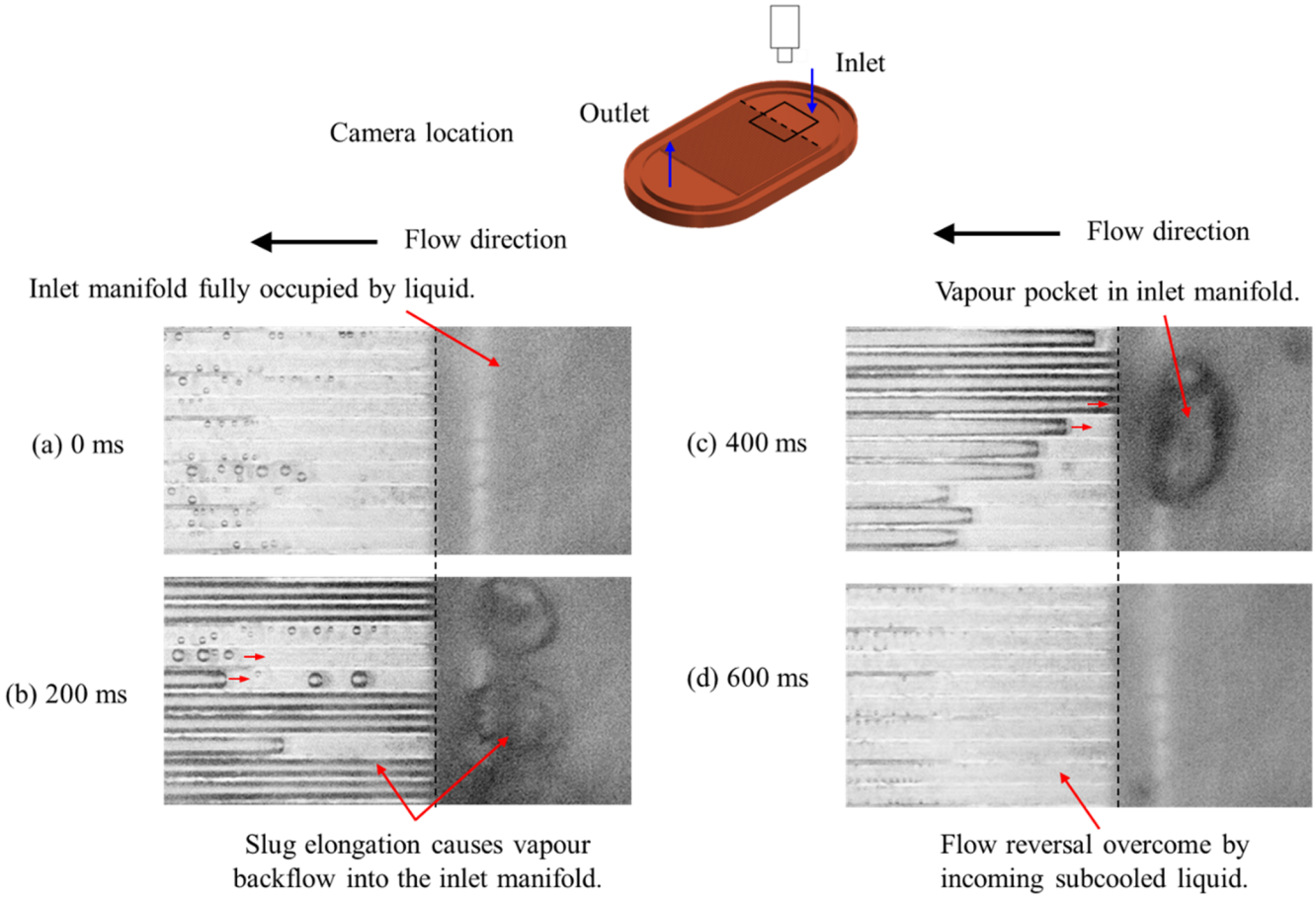

Fig. 13. Flow reversal captured at the channel inlet and conditions P = 1 bar, G = 300 kg/m^2 s, $q_w^{"}$ = 24.8 kW/m^2 and ΔT_{sub} = 10 K.

the observation of Bogojevic et al. [34] and Deng et al. [35] who found higher flow oscillations at higher degrees of subcooling in their parallel channel heat sinks. This could be because both studies used water as the working fluid and annular flow was the predominant flow pattern in the heat sink. Bogojevic et al. [34] attributed the lower flow oscillations to improved flow distribution at higher inlet water temperatures in the heat sink.

In summary, a complex dependency of two-phase flow instability on the degree of subcooling was observed. Increasing the degree of subcooling resulted in a reduction in pressure drop fluctuations when the flow was dominated by slug flow. On the other hand, when heat flux was increased and annular flow dominated in the channels, increasing inlet subcooling increased the pressure fluctuations, although only slightly.

3.2.4. Effect on heat transfer rates

Local heat transfer coefficients were measured at five locations along the middle of the heat sink and in order to assess the effect of subcooling on heat transfer separately in the subcooled and saturated boiling region of the channels, the local heat transfer trends at the three subcooling conditions are plotted in Figs. 14–16 for wall heat fluxes $q_w^{"}$ ~ 52 kW/m^2, $q_w^{"}$ ~ 107 kW/m^2 and $q_w^{"}$ ~ 161 kW/m^2 respectively. The wall heat fluxes selected represent the low, medium and high heat flux condition. The empty markers represent subcooled flow boiling heat transfer coefficients while the filled markers denote flow boiling heat transfer coefficients in the saturated region. At a given wall heat flux condition, increasing inlet subcooling decreases the local vapour quality along the channels due to the extension of the subcooled region at higher inlet subcooling.

Local heat transfer coefficients rose sharply in the subcooled region and generally peaked at the location of boiling incipience. The sharp rising trend of heat transfer coefficients in the subcooled region is also an indication of subcooled boiling, which was also confirmed by flow visualisation. After the initial peak at the onset of boiling, the local heat transfer trend decreases moderately along the channel with increasing local vapour quality, also observed in Al-Zaidi et al. [63] using a similar fluid, HFE-7100, and Choi et al. [64], but recovers slightly near the channel exit.

Bubbly flow was typically observed in the subcooled region as well as near the location of boiling incipience. As a result, the nucleate boiling mechanism may be reasonably assumed to dominate in this region. The high heat transfer coefficients could thus be due to the high heat transfer rates arising from micro-layer evaporation underneath nucleating bubbles, as mentioned in Mahmoud and Karayiannis [19] combined with the micro-convection currents induced in the bulk fluid surrounding a nucleating bubble as it departs its nucleation site. The subsequent reduction in local heat transfer coefficients along the channel could be attributed to the suppression of bubble nucleation sites, which has been observed in slug flow. Naturally, the periodic suppression of nucleation cavities reduces the time-averaged heat transfer coefficient at a given location on the channels. Heat transfer coefficients increase again near the exit of the channels, which could be caused by liquid film thinning during thin-film evaporation in the slug and annular flow regime or due to small heat losses to the outlet plenum.

In the subcooled region, increasing inlet subcooling generally resulted in a reduction in heat transfer coefficients, evident from Figs. 14 and 15 at ΔT_{sub} = 10 K and 20 K. This is in agreement with the trends reported by Agostini et al. [37]. It could be attributed to higher bubble departure frequencies and shorter waiting times between successive

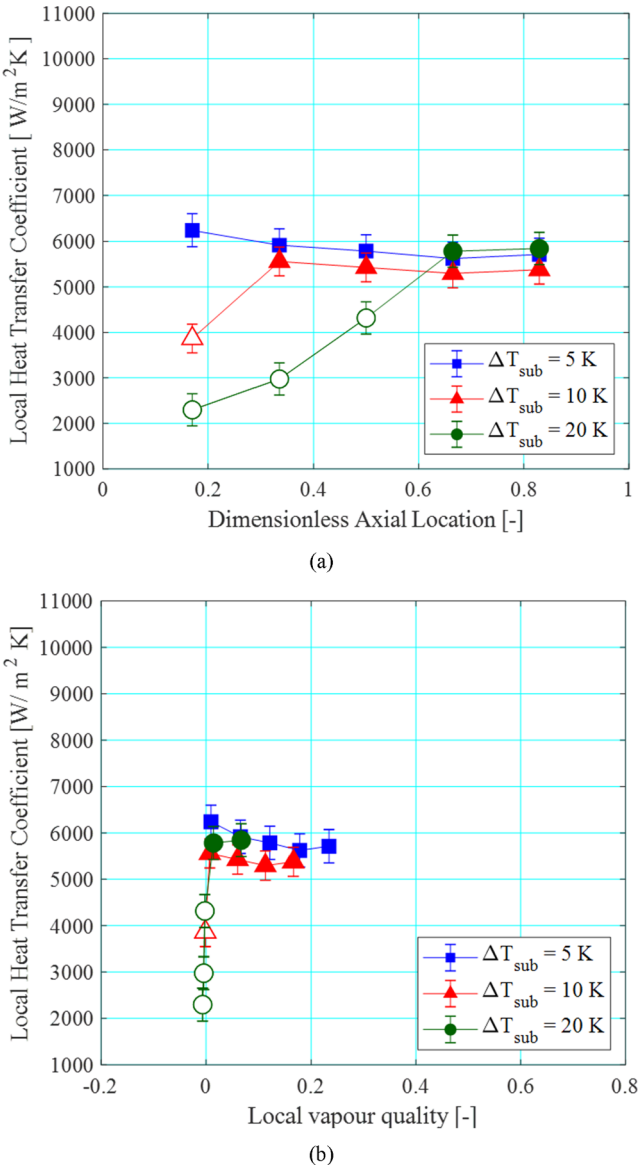

Fig. 14. Local heat transfer coefficients along the heat sink at P = 1 bar, G = 200 kg/m^2 s and $q_w^{"}$ ~ 52 kW/m^2. Empty and filled markers denote heat transfer coefficients measured in the subcooled and saturated boiling region respectively.

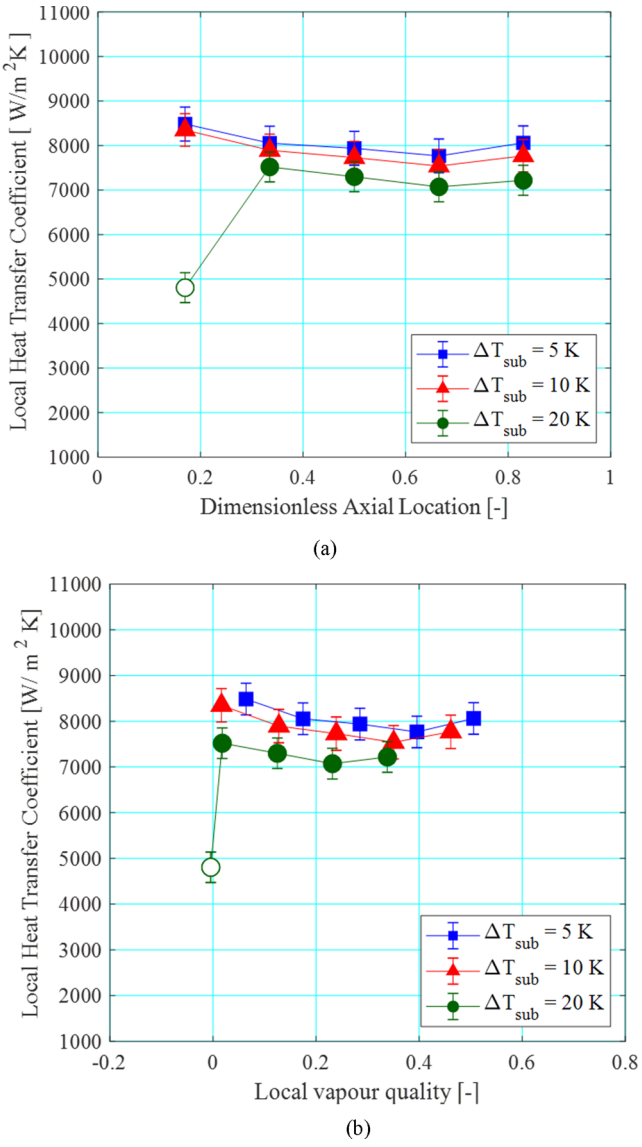

Fig. 15. Local heat transfer coefficients along the heat sink at P = 1 bar, G = 200 kg/m^2 s and $q_w^{"}$ ~ 107 kW/m^2. Empty and filled markers denote heat transfer coefficients measured in the subcooled and saturated boiling region respectively.

bubble ebullition cycles at lower subcooling, as higher bulk liquid temperatures will inevitably require a shorter time period to reach the sufficient wall superheat degree for bubble nucleation.

At the low heat flux condition, flow boiling heat transfer coefficients in the saturated boiling region at ΔT_{sub} = 20 K were marginally higher than that at ΔT_{sub} = 5 K and 10 K, see Fig. 14. At this heat flux, bubbly flow was observed in the channels at ΔT_{sub} = 20 K while slug as well as churn flow have already developed in the channels at ΔT_{sub} = 5 K and 10 K. The high saturated flow boiling heat transfer coefficients observed at the highest inlet subcooling condition could be due to the presence and dominance of nucleate boiling near the location of boiling incipience. The predominance of bubbly flow in the channels at this condition also supports this observation. As slug and churn flow tend to suppress some nucleation activity on the channel walls, the contribution of the nucleate boiling mechanism is reduced, and thus slightly lower heat transfer coefficients are observed at ΔT_{sub} = 10 K at this heat flux level. Increasing inlet subcooling resulted in a small reduction in heat transfer coefficients in the saturated boiling region. This is more apparent in Figs. 15(b) and 16(b), i.e. medium and high heat fluxes, where the local heat transfer trend is plotted with respect to vapour quality.

As shown in Fig. 11, the range of active nucleation sites become smaller with increasing subcooling. This indicates lower bubble generation frequency in the channels at higher subcooling, i.e. lower nucleate boiling heat transfer coefficients at higher subcooling. Additionally, whilst delayed flow pattern transitions were observed at higher inlet subcooling conditions, see Table 3, at medium to high heat fluxes, annular flow was observed at all subcooling degrees in the channels. Heat transfer coefficients have been demonstrated to increase with vapour quality in the annular flow regime in Costa-Patry et al. [65], Huang and Thome [39] and Falsetti et al. [66]. A combination of lower nucleate boiling heat transfer coefficients (due to reduced bubble generation activity) and lower contribution of thin-film evaporation (due to delayed flow regime transition to annular flow) to total heat transfer could explain the lower heat transfer coefficients observed in the saturated region at higher degrees of inlet subcooling. Evidently, varying the degree of inlet subcooling by 5–20 K has an effect on flow

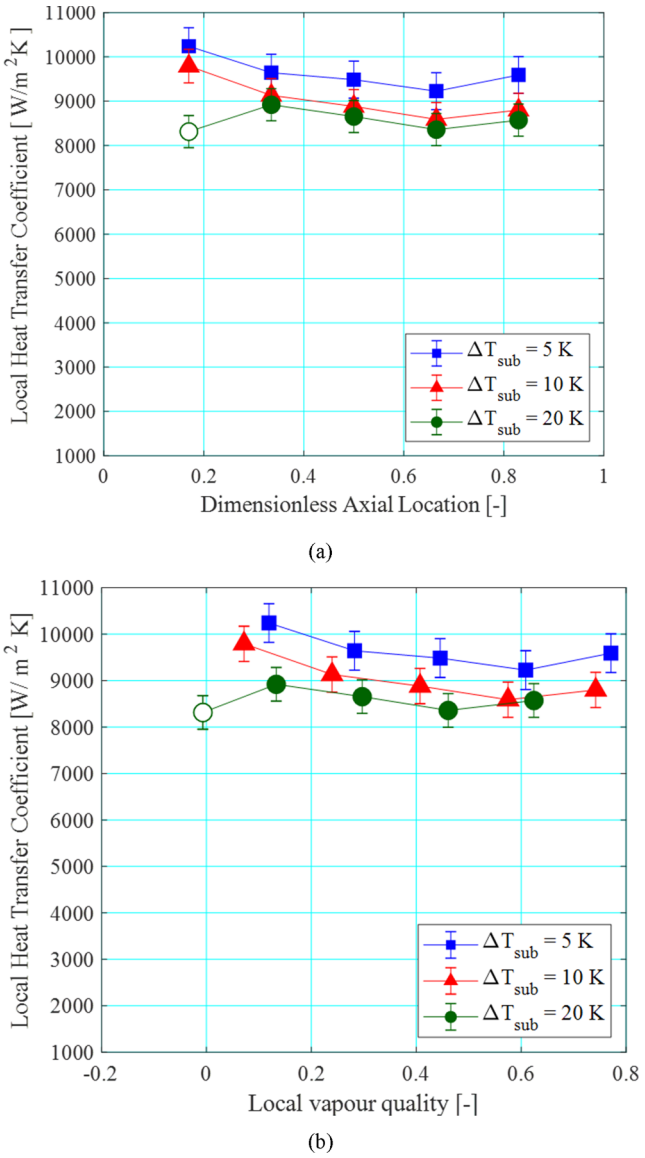

Fig. 16. Local heat transfer coefficients along the heat sink at P = 1 bar, G = 200 kg/m^2 s and $q_w^{"}$ ~ 161 kW/m^2. Empty and filled markers denote heat transfer coefficients measured in the subcooled and saturated boiling region respectively.

boiling heat transfer coefficients, although small (i.e about ± 10%) in the saturated boiling region, as also concluded by studies in [26,37,38].

The effect of inlet subcooling on the average heat transfer coefficients in the heat sink is depicted in Fig. 17. Note that the average heat transfer coefficients referred to here are averaged from heat transfer coefficients along the channel and includes the local heat transfer coefficient in the subcooled region, according to Eq. (30). The average heat transfer coefficient increases with decreasing inlet subcooling. At the lowest heat flux condition, the rise in the average heat transfer coefficients in the channel at lower inlet subcooling conditions is more pronounced.

As mentioned earlier (see Fig. 10), increasing the degree of inlet subcooling at a given wall heat flux increases the length of the subcooled region in the channels. Although the local heat transfer coefficients in the subcooled region rises steeply along the channel, its magnitude is lower than heat transfer coefficients typically observed in the saturated boiling region. Consequently, the average heat transfer coefficient along the entire length of the channel is lower at high subcooling for a given wall heat flux condition in the heat sink. From Fig. 10, it is clear that the subcooled region constitutes a substantial portion of the total channel length at wall heat fluxes $q_w^{"}$ ~ 26 kW/m^2 to 52 kW/m^2. As a result, the subcooled heat transfer coefficient has a larger contribution to the overall heat transfer coefficients in the channel. Hence a stronger effect of subcooling is observed in the low heat flux region.

Overall, the effect of subcooling on local heat transfer coefficients was found to be more pronounced in the subcooled region where subcooled boiling was observed. This was attributed to higher bubble departure frequencies and shorter waiting times between successive bubble ebullition cycles at lower subcooling. The effect of subcooling was generally smaller in the saturated boiling region. Similarly, average heat transfer coefficients exhibited a strong dependency on the degree of inlet subcooling, particularly at low wall heat fluxes, due to the substantial length of the subcooled region. The subcooled length decreases with heat flux, and as a result the effect of inlet subcooling is smaller with increasing wall heat flux.

3.2.5. *Effect on pressure drop*

Fig. 18(a) depicts the total pressure drop in the channels (i.e. ΔP_{ch}, see Eq. (2)) – including the single and two-phase pressure drop –as a function of wall heat flux at three inlet subcooling conditions. The pressure drop in the two-phase region (i.e. ΔP_{tp}, see Eq. (18)) at the same conditions are shown in Fig. 18(b). Note that the two-phase pressure drop at the lowest wall heat flux condition, i.e. $q_w^{"}$ = 26 kW/m^2, is zero as the channels were entirely subcooled at ΔT_{sub} = 20 K.

As expected, channel pressure drop increases with wall heat flux due to an increase in overall void fraction in the channels, which is associated with higher flow resistance at higher heat fluxes [51]. Channel pressure drop generally decreased with increasing inlet subcooling, particularly when ΔT_{sub} = 20 K. Additionally, comparing Fig. 18(a) and (b), it is clear that the contribution of single-phase pressure drop is only significant at low wall heat fluxes. The effect of inlet subcooling on channel pressure drop was more significant at wall heat fluxes below $q_w^{"}$ = 52 kW/m^2, due to the substantial length of the subcooled region in the channel array, see Fig. 10. This is partly because the single-phase liquid pressure drop, which is much smaller compared to two-phase pressure drop, has a larger contribution to total pressure drop in the channel at higher degrees of subcooling, due to the longer subcooled length in the channels. Similar observations were also reported in Deng et al. [29] and Chen et al. [27].

Similarly, the effect of inlet subcooling on two-phase pressure drop

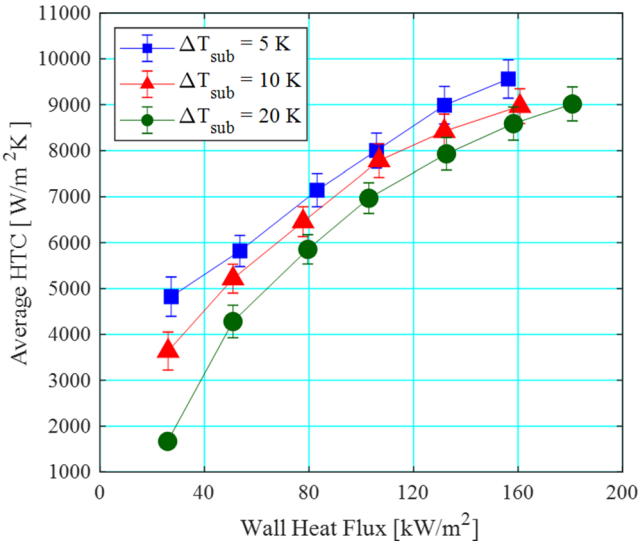

Fig. 17. Effect of inlet subcooling on average heat transfer coefficients along the channel for wall heat fluxes between $q_w^{"}$ = 25.9–180.7 kW/m^2 at P = 1 bar and G = 200 kg/m^2 s.

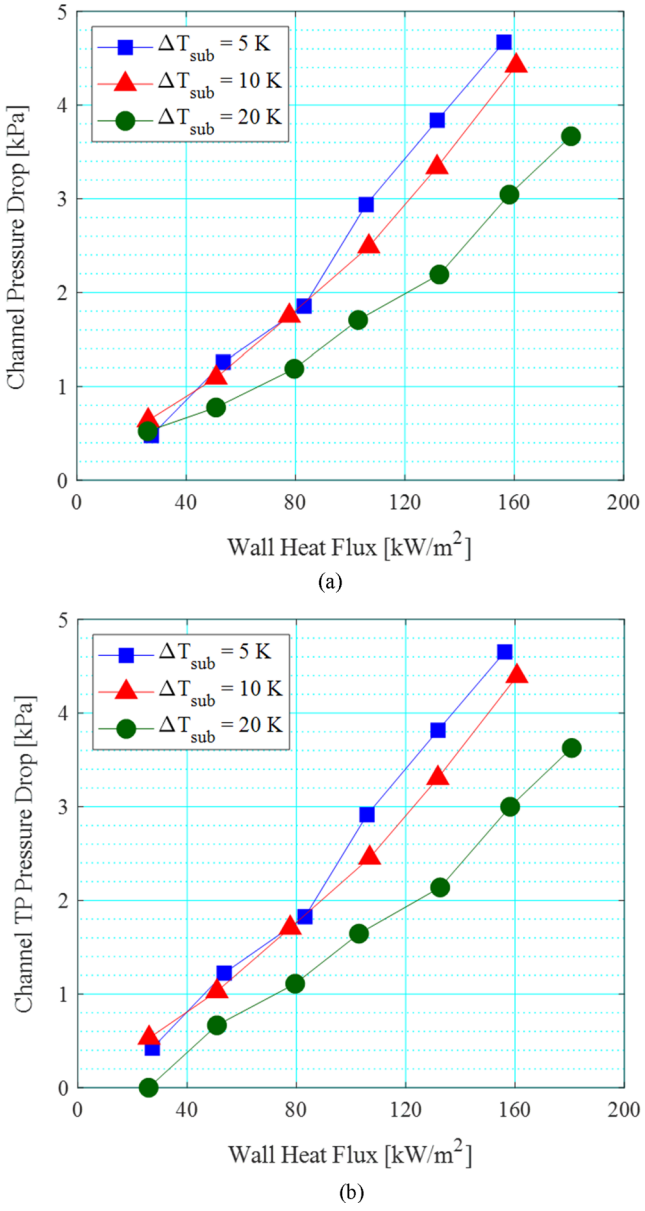

Fig. 18. Effect of subcooling on (a) total pressure drop in the channel (single and two-phase) and (b) two-phase pressure drop in the channel for wall heat fluxes $q_w^{"}$ = 25.9–180.7 kW/m^2 at P = 1 bar and G = 200 kg/m^2 s. Error bars are ± 0.1% to ± 0.3% and are too small to be visible on the graph.

was negligible between ΔT_{sub} = 5 K and ΔT_{sub} = 10 K, especially at wall heat fluxes below $q_w^{"}$ = 83 kW/m^2. On the other hand, at a given wall heat flux condition, the magnitude of the two-phase pressure drop at ΔT_{sub} = 20 K is notably smaller compared to lower degrees of inlet subcooling.

As mentioned above, flow pattern transitions occurred at higher vapour qualities (summarised in Table 3) with increasing degrees of inlet subcooling, particularly at ΔT_{sub} = 20 K. This was attributed to less vigorous bubble coagulation in the channels due to the condensation of bubbles in the subcooled region, which was extended with higher inlet subcooling at a given wall heat flux condition. This could also have contributed to a smaller void fraction in the channels at higher degrees of subcooling for a nominal wall heat flux level. Furthermore, Fig. 11 predicts a smaller range of active nucleation sites at higher degrees of inlet subcooling, which may also indicate a smaller channel void fraction as a direct result of lower bubble nucleation activity in the channels at higher degrees of subcooling. As both the acceleration component in two-phase pressure drop is strongly dependent on the void fraction [51], the smaller void fraction at larger inlet subcooling could have resulted in the lower two-phase pressure drop in the heat sink.

Pressure drop characteristics were found to be affected by changes in the degree of subcooling. Increasing the inlet subcooling decreased both the total pressure drop and two-phase pressure drop in the channels (i.e. ΔP_{ch} and ΔP_{tp} respectively), particularly when the subcooling was increased to ΔT_{sub} = 20 K. The reduction in pressure drop values was attributed to the delay in flow pattern development and smaller channel void fraction with increase in the degrees of subcooling.

4. Conclusions

The effect of inlet subcooling on the heat transfer and pressure drop characteristics of dielectric fluid HFE-7200 in a multi-microchannel heat sink was investigated. Flow boiling experiments were conducted at three inlet subcooling conditions, i.e. ΔT_{sub} = 5 K, 10 K and 20 K, at P = 1 bar and G = 200 kg/m^2 s for wall heat fluxes in the range of $q_w^{"}$ = 25.9 to 180.7 kW/m^2. The equivalent base heat fluxes were between $q_b^{"}$ = 99.1 to 605.3 kW/m^2.

Increasing system subcooling generally delayed flow pattern transitions in the channel to higher quality values. This was attributed to the extended subcooled region in the channels and lower rate of bubble coalescence at higher system subcooling. Furthermore, increasing system subcooling narrowed the range of active cavity sizes, which could indicate lower bubble generation frequencies at higher inlet subcooling, also affecting flow pattern development. The effect of subcooling on flow pattern development subsequently affected two-phase instabilities, heat transfer as well as pressure drop behaviour in the microchannel heat sink.

The effect of degree of subcooling on flow instability depended on the prevailing flow regimes. Pressure drop oscillations were associated to flow reversal triggered by the rapid expansion of vapour slugs in the heat sink. Increasing inlet subcooling reduced the magnitude of flow oscillations due to the delay in slug flow formation. Lower pressure drop oscillations were observed at heat fluxes where annular flow was dominant. Increasing system subcooling in this region increased the magnitude of oscillations slightly.

The dependency of local heat transfer coefficients in the subcooled region on system subcooling was stronger compared to the saturated boiling region of the channels. The average heat transfer coefficient of the heat sink decreased with increasing subcooling, especially at low heat fluxes, due to the substantial length of the subcooled region. The effect of inlet subcooling on average heat transfer coefficient becomes less with increasing heat flux, since the subcooled region shrunk with heat flux and thus exerted a smaller contribution to the overall heat transfer.

Increasing the degree of subcooling also lowered the total and two-phase pressure drop in the heat sink, in particular at ΔT_{sub} = 20 K, at a nominal wall heat flux condition. This was mainly attributed to delayed flow pattern transition and smaller channel void fraction at larger subcooling.

The above observations help elucidate the effect of subcooling on flow instability, flow patterns, heat transfer rates and pressure drop and provide one possible explanation for discrepancies reported in past studies. The work indicates clearly that the degree of subcooling should be identified if experimental results are to be compared. The effect of the degree of subcooling on the critical heat flux was not examined as our range did not cover the occurrence of critical heat flux. Further work is also recommended in this area and should include different fluids.

Declaration of Competing Interest

The authors declare that they have no known competing financial interests or personal relationships that could have appeared to influence the work reported in this paper.

Acknowledgement

The authors would like to thank TMD Technologies Ltd. for their financial support of the project. The technical support of Costas Xanthos when constructing the test rig is gratefully acknowledged.

References

[1] T.G. Karayiannis, M.M. Mahmoud, Flow boiling in microchannels: fundamentals and applications, Appl. Therm. Eng. 115 (2017) 1372–1397.
[2] I. Mudawar, Assessment of high-heat-flux thermal management schemes, IEEE Trans. Components Packag. Technol. 24 (2) (2001) 122–141.
[3] P. Zhou, J. Horn, G. Upadhya, K. Goodson, M. Munch, Electro-kinetic microchannel cooling system for desktop computers, Annu. IEEE Semicond. Therm. Meas. Manag. Symp. 20 (2004) 26–29.
[4] J.F. Tullius, R. Vajtai, Y. Bayazitoglu, A review of cooling in microchannels, Heat Transf. Eng. 32 (7–8) (2011) 527–541.
[5] S. Krishnan, S.V. Garimella, G.M. Chrysler, R.V. Mahajan, Towards a thermal Moore's law, IEEE Trans. Adv. Packag. 30 (3) (2007) 462–474.
[6] D.B. Tuckerman, R.F.W. Pease, High-performance heat sinking for VLSI, IEEE Electron Device Lett. 2 (5) (1981) 126–129.
[7] E.G. Colgan, B. Furman, M. Gaynes, N. LaBianca, J.H. Magerlein, R. Polastre, R. Bezama, K. Marston, R. Schmidt, High performance and subambient silicon microchannel cooling, J. Heat Transf. 129 (8) (2007) 1046–1051.
[8] W. Escher, T. Brunschwiler, B. Michel, D. Poulikakos, Experimental investigation of an ultrathin manifold microchannel heat sink for liquid-cooled chips, J. Heat Transfer 132 (8) (2010) 1–10.
[9] H.Y.Y. Zhang, D. Pinjala, T.N.N. Wong, K.C.C. Toh, Y.K.K. Joshi, Single-phase liquid cooled microchannel heat sink for electronic packages, Appl. Therm. Eng. 25 (10) (2005) 1472–1487.
[10] J.R. Thome, A. Cioncolini, Flow boiling in microchannels, Adv. Heat Transf. 49 (January 2017) (2017) 157–224.
[11] J. Lee, I. Mudawar, Fluid flow and heat transfer characteristics of low temperature two-phase micro-channel heat sinks – Part 1: Experimental methods and flow visualization results, Int. J. Heat Mass Transf. 51 (17–18) (2008) 4315–4326.
[12] K.P. Drummond, D. Back, M.D. Sinanis, D.B. Janes, D. Peroulis, J.A. Weibel, S.V. Garimella, A hierarchical manifold microchannel heat sink array for high-heat-flux two-phase cooling of electronics, Int. J. Heat Mass Transf. 117 (2018) 319–330.
[13] S.N. Joshi, D.J. Lohan, E.M. Dede, Two-phase performance of a hybrid jet plus multipass microchannel heat sink, J. Therm. Sci. Eng. Appl. 12 (1) (2020).
[14] M. Visaria, I. Mudawar, Application of two-phase spray cooling for thermal management of electronic devices, IEEE Trans. Components Packag. Technol. 32 (4) (2009) 784–793.
[15] X. Gao, R. Li, Spray impingement cooling: the state of the art, Advanced Cooling Technologies and Applications, IntechOpen, 2019.
[16] S.G. Kandlikar, History, advances, and challenges in liquid flow and flow boiling heat transfer in microchannels: a critical review, J. Heat Transf. 134 (3) (2012).
[17] L. Cheng, G. Xia, Fundamental issues, mechanisms and models of flow boiling heat transfer in microscale channels, Int. J. Heat Mass Transf. 108 (2017) 97–127.
[18] V.V. Kuznetsov, Fundamental issues related to flow boiling and two-phase flow patterns in microchannels – experimental challenges and opportunities, Heat Transf. Eng. 40 (9–10) (2019) 711–724.
[19] M.M. Mahmoud, T.G. Karayiannis, Flow boiling in mini to microdiameter channels, in: J.R. Thome (Ed.), Encyclopedia of Two-Phase Heat Transfer and Flow IV, World Scientific Publishing, 2018, pp. 233–301. (Chapter 4) https://doi.org/10.1142/9789813234444_0004.
[20] T.G. Karayiannis, M.M. Mahmoud, D.B.R. Kenning, A study of discrepancies in flow boiling results in small to microdiameter metallic tubes, Exp. Therm Fluid Sci. 36 (2012) 126–142.
[21] Y.Y. Hsu, On the size range of active nucleation cavities on a heating surface, J. Heat Transf. 84 (3) (1962) 207–213.
[22] S.G. Kandlikar, Nucleation characteristics and stability considerations during flow boiling in microchannels, Exp. Therm Fluid Sci. 30 (5) (2006) 441–447.
[23] D. Euh, B. Ozar, T. Hibiki, M. Ishii, C.-H. Song, Characteristics of bubble departure frequency in a low-pressure subcooled boiling flow, J. Nucl. Sci. Technol. 47 (7) (2010) 608–617.
[24] P. Goel, A.K. Nayak, P. Ghosh, J.B. Joshi, Experimental study of bubble departure characteristics in forced convective subcooled nucleate boiling, Exp. Heat Transf. 31 (3) (2018) 194–218.
[25] J. Lee, I. Mudawar, Fluid flow and heat transfer characteristics of low temperature two-phase micro-channel heat sinks – Part 2. Subcooled boiling pressure drop and heat transfer, Int. J. Heat Mass Transf. 51 (17–18) (2008) 4327–4341.
[26] C.L. Ong, J.R. Thome, Flow boiling heat transfer of R134a, R236fa and R245fa in a horizontal 1.030 mm circular channel, Exp. Therm Fluid Sci. 33 (4) (2009) 651–663.
[27] J. Chen, S. Zhang, Y. Tang, H. Chen, W. Yuan, J. Zeng, Effect of operational parameters on flow boiling heat transfer performance for porous interconnected microchannel nets, Appl. Therm. Eng. 121 (2017) 443–453.
[28] S. Zhang, W. Yuan, Y. Tang, J. Chen, Z. Li, Enhanced flow boiling in an interconnected microchannel net at different inlet subcooling, Appl. Therm. Eng. 104 (2016) 659–667.
[29] D. Deng, W. Wan, H. Shao, Y. Tang, J. Feng, J. Zeng, Effects of operation parameters on flow boiling characteristics of heat sink cooling systems with reentrant porous microchannels, Energy Convers. Manag. 96 (2015) 340–351.
[30] D. Deng, L. Chen, W. Wan, T. Fu, X. Huang, Flow boiling performance in pin fin-interconnected reentrant microchannels heat sink in different operational conditions, Appl. Therm. Eng. 150 (2019) 1260–1272.
[31] J. Zeng, S. Zhang, Y. Tang, Y. Sun, W. Yuan, Flow boiling characteristics of micro-grooved channels with reentrant cavity array at different operational conditions, Int. J. Heat Mass Transf. 114 (2017) 1001–1012.
[32] Y.K. Prajapati, P. Bhandari, Flow boiling instabilities in microchannels and their promising solutions – a review, Exp. Therm Fluid Sci. 88 (2017) 576–593.
[33] S. Lee, V.S. Devahdhanush, I. Mudawar, Frequency analysis of pressure oscillations in large length-to-diameter two-phase micro-channel heat sinks, Int. J. Heat Mass Transf. 116 (2018) 273–291.
[34] D. Bogojevic, K. Sefiane, A.J. Walton, H. Lin, G. Cummins, Two-phase flow instabilities in a silicon microchannels heat sink, Int. J. Heat Fluid Flow 30 (2009) 854–867.
[35] D. Deng, W. Wan, Y. Qin, J. Zhang, X. Chu, Flow boiling enhancement of structured microchannels with micro pin fins, Int. J. Heat Mass Transf. 105 (2017) 338–349.
[36] T.A. Kingston, J.A. Weibel, S.V. Garimella, High-frequency thermal-fluidic characterization of dynamic microchannel flow boiling instabilities: Part 2 – Impact of operating conditions on instability type and severity, Int. J. Multiph. Flow 106 (2018) 189–201.
[37] B. Agostini, J.R. Thome, M. Fabbri, B. Michel, D. Calmi, U. Kloter, High heat flux flow boiling in silicon multi-microchannels – Part II: Heat transfer characteristics of refrigerant R245fa, Int. J. Heat Mass Transf. 51 (21–22) (2008) 5415–5425.
[38] C.L. Ong, J.R. Thome, Macro-to-microchannel transition in two-phase flow: Part 2 – Flow boiling heat transfer and critical heat flux, Exp. Therm Fluid Sci. 35 (6) (2011) 873–886.
[39] H. Huang, J.R. Thome, Local measurements and a new flow pattern based model for subcooled and saturated flow boiling heat transfer in multi-microchannel evaporators, Int. J. Heat Mass Transf. 103 (2016) 701–714.
[40] L. Yin, P. Jiang, R. Xu, H. Hu, L. Jia, Heat transfer and pressure drop characteristics of water flow boiling in open microchannels, Int. J. Heat Mass Transf. 137 (2019) 204–215.
[41] R. Revellin, J.R. Thome, A theoretical model for the prediction of the critical heat flux in heated microchannels, Int. J. Heat Mass Transf. 51 (5–6) (2008) 1216–1225.
[42] B. Agostini, R. Revellin, J.R. Thome, M. Fabbri, B. Michel, D. Calmi, U. Kloter, High heat flux flow boiling in silicon multi-microchannels – Part III: Saturated critical heat flux of R236fa and two-phase pressure drops, Int. J. Heat Mass Transf. 51 (21–22) (2008) 5426–5442.
[43] H. Huang, N. Borhani, J.R. Thome, Experimental investigation on flow boiling pressure drop and heat transfer of R1233zd(E) in a multi-microchannel evaporator, Int. J. Heat Mass Transf. 98 (2016) 596–610.
[44] J. Lee, I. Mudawar, Critical heat flux for subcooled flow boiling in micro-channel heat sinks, Int. J. Heat Mass Transf. 52 (13–14) (2009) 3341–3352.
[45] R. Remsburg, Thermal Design of Electronic Equipment, 2001.
[46] R.J. Phillips, Forced Convection, Liquid Cooled, Microchannel Heat Sinks, Massachusetts Institute of Technology, 1987.
[47] F.P. Incropera, T.L. Bergman, D.P. DeWitt, A.S. Lavine, Fundamentals of Heat and Mass Transfer, seventh ed., John Wiley & Sons, 2012.
[48] K. Mishima, T. Hibiki, Some characteristics of air-water two-phase flow in small diameter vertical tubes, Int. J. Multiph. Flow 22 (4) (1996) 703–712.
[49] H. Huang, J.R. Thome, An experimental study on flow boiling pressure drop in multi-microchannel evaporators with different refrigerants, Exp. Therm Fluid Sci. 80 (2017) 391–407.
[50] R.K. Shah, A.L. London, Laminar Flow Forced Convection in Ducts: A Source Book for Compact Heat Exchanger Analytical Data, first ed., Academic Press, 1978.
[51] John G. Collier, John R. Thome, Convective Boiling and Condensation, third ed., Clarendon Press, 1996.
[52] D. Chisholm, Two-phase flow in bends, Int. J. Multiph. Flow 6 (4) (1980) 363–367.
[53] D. Chisholm, Two-phase flow in heat exchangers and pipelines, Heat Transf. Eng. 6 (2) (1985) 48–57.
[54] A. Kawahara, P.Y. Chung, M. Kawaji, Investigation of two-phase flow pattern, void fraction and pressure drop in a microchannel, Int. J. Multiph. Flow 28 (9) (2002) 1411–1435.
[55] W. Hugh, W. Coleman, Glenn, Steele, Experimentation, Validation, and Uncertainty Analysis for Engineers, third ed., John Wiley & Sons, 2009.
[56] X.F. Peng, G.P. Peterson, Convective heat transfer and flow friction for water flow in microchannel structures, Int. J. Heat Mass Transf. 39 (12) (1996) 2599–2608.
[57] K. Stephan, P. Preusser, Wärmeűbergang Und Maximale Wärmstromichte Beim Behältersieden Binärer Und Ternärer Flűssigkeitsgemische, Chem. Ing. Tech. 51 (37) (1979).
[58] Y. Liu, D.F. Fletcher, B.S. Haynes, On the importance of upstream compressibility in microchannel boiling heat transfer, Int. J. Heat Mass Transf. 58 (1–2) (2013) 503–512.
[59] S. Gedupudi, D.B.R. Kenning, T.G. Karayiannis, Flow boiling in rectangular microchannels: 1-D modeling of the influence of inlet resistance on flow reversal, Heat Transf. Eng. 37 (13–14) (2016) 1114–1125.
[60] A.H.M. Al-Zaidi, Flow Boiling and Condensation with Refrigerant HFE-7100 for

Cooling High Heat Flux Devices, Ph.D Thesis Brunel University London, 2019.
[61] Omega Engineering, Micro-Machined Silicon Wet/Wet Differential Pressure Transducers. [Online]. Available: https://www.omega.co.uk/pptst/PX409-WWDIF.html. [accessed: 20-Apr-2020].
[62] TC Ltd., Mineral Insulated Thermocouples – Type 12, 2019.
[63] A.H. Al-Zaidi, M.M. Mahmoud, T.G. Karayiannis, Flow boiling of HFE-7100 in microchannels: experimental study and comparison with correlations, Int. J. Heat Mass Transf. 140 (2019) 100–128.
[64] Y.-S. Choi, T. Lim, S.-S. You, H.-S. Kim, Two-phase flow boiling heat transfer of FC-72 in parallel micro-channels, Exp. Heat Transf. 30 (4) (2017) 284–301.
[65] E. Costa-Patry, J. Olivier, B. Michel, J.R. Thome, Two-phase flow of refrigerants in 85 μm-wide multi-microchannels: Part II – Heat transfer with 35 local heaters, Int. J. Heat Fluid Flow 32 (2) (2011) 464–476.
[66] C. Falsetti, H. Jafarpoorchekab, M. Magnini, N. Borhani, J.R. Thome, Two-phase operational maps, pressure drop, and heat transfer for flow boiling of R236fa in a micro-pin fin evaporator, Int. J. Heat Mass Transf. 107 (2017) 805–819.